Monthly Notices of the ROYAL ASTRONOMICAL SOCIETY

MNRAS **512,** 3195–3214 (2022)
Advance Access publication 2022 March 17

https://doi.org/10.1093/mnras/stac723

The Lick Observatory Supernova Search follow-up program: photometry data release of 70 SESNe

WeiKang Zheng,[1]★ Benjamin E. Stahl,[1,2] Thomas de Jaeger,[1,3] Alexei V. Filippenko,[1,4] Shan-Qin Wang,[5] Wen-Pei Gan,[5] Thomas G. Brink,[1] Ivan Altunin,[1] Raphael Baer-Way,[1] Andrew Bigley,[1] Kyle Blanchard,[1] Peter K. Blanchard,[6] James Bradley,[1] Samantha K. Cargill,[1] Chadwick Casper,[1] Teagan Chapman,[1] Vidhi Chander,[1] Sanyum Channa,[2,7] Byung Yun Choi,[1] Nick Choksi,[1] Matthew Chu,[2] Kelsey I. Clubb,[1] Daniel P. Cohen,[8] Paul A. Dalba,[9,10] Asia deGraw,[1] Maxime de Kouchkovsky,[1] Michael Ellison,[1] Edward Falcon,[1] Ori D. Fox,[11] Kiera Fuller,[1] Mohan Ganeshalingam,[12] Nachiket Girish,[2] Carolina Gould,[1] Goni Halevi,[1,13] Andrew Halle,[1] Kevin T. Hayakawa,[8] Romain Hardy,[8] Julia Hestenes,[1] Andrew M. Hoffman,[1] Michael Hyland,[1] Benjamin T. Jeffers,[1] Connor Jennings,[1] Michael T. Kandrashoff,[1] Anthony Khodanian,[1] Minkyu Kim,[1] Haejung Kim,[1] Michelle E. Kislak,[1,14] Daniel Krishnan,[1] Sahana Kumar,[1,15] Snehaa Ganesh Kumar,[1] Joel Leja,[16,17,18] Erin J. Leonard,[1,19] Gary Z. Li,[20] Weidong Li,[1]† Ji-Shun Lian,[5] Evelyn Liu,[1] Thomas B. Lowe,[3] Philip Lu,[21] Emily Ma,[1] Michelle N. Mason,[22] Michael May,[1] Kyle McAllister,[1] Emma McGinness,[1] Shaunak Modak,[2,13] Jeffrey Molloy,[1] Yukei S. Murakami,[23] Omnarayani Nayak,[11] Derek Perera,[1] Kenia Pina,[1] Druv Punjabi,[1] Andrew Rikhter,[24] Timothy W. Ross,[1] Jackson Sipple,[1] Costas Soler,[1] Samantha Stegman,[1,25] Haynes Stephens,[1] James Sunseri,[1,2] Kevin Tang,[1] Stephen Taylor,[1] Patrick Thrasher,[1] Schuyler D. Van Dyk,[26] Xiang-Gao Wang,[5] Jeremy Wayland,[1] Andrew Wilkins,[1] Abel Yagubyan,[1] Heechan Yuk,[27] Sameen Yunus[1] and Keto D. Zhang[1]

Affiliations are listed at the end of the paper

Accepted 2022 March 9. Received 2022 March 9; in original form 2022 January 5

ABSTRACT

We present *BVRI* and unfiltered (*Clear*) light curves of 70 stripped-envelope supernovae (SESNe), observed between 2003 and 2020, from the Lick Observatory Supernova Search follow-up program. Our SESN sample consists of 19 spectroscopically normal SNe Ib, 2 peculiar SNe Ib, six SNe Ibn, 14 normal SNe Ic, 1 peculiar SN Ic, 10 SNe Ic-BL, 15 SNe IIb, 1 ambiguous SN IIb/Ib/c, and 2 superluminous SNe. Our follow-up photometry has (on a per-SN basis) a mean coverage of 81 photometric points (median of 58 points) and a mean cadence of 3.6 d (median of 1.2 d). From our full sample, a subset of 38 SNe have pre-maximum coverage in at least one passband, allowing for the peak brightness of each SN in this subset to be quantitatively determined. We describe our data collection and processing techniques, with emphasis toward our automated photometry pipeline, from which we derive publicly available data products to enable and encourage further study by the community. Using these data products, we derive host-galaxy extinction values through the empirical colour evolution relationship and, for the first time, produce accurate rise-time measurements for a large sample of SESNe in both optical and infrared passbands. By modelling multiband light curves, we find that SNe Ic tend to have lower ejecta masses and lower ejecta velocities than SNe Ib and IIb, but higher ^{56}Ni masses.

Key words: supernovae: general – galaxies: distances and redshifts.

1 INTRODUCTION

It is well established that massive stars (i.e. those having $M \gtrsim 8\,M_{\odot}$) have short lives that end in catastrophic explosions known as core-collapse supernovae (CCSNe). Among CCSNe, those whose spectra show features of hydrogen are classified as Type II SNe (see, e.g. Filippenko 1997; Gal-Yam 2017 for reviews of SN classification). In contrast, hydrogen-poor CCSNe are classified as Type Ib or Ic, depending on whether their optical spectra contain obvious helium features (Matheson 2001). The progenitor stars of hydrogen-poor CCSNe have their outer envelopes stripped away before explosion by strong winds during the Wolf–Rayet phase (e.g. Conti 1975; Smith &

★ E-mail: zwk@astro.berkeley.edu
† Deceased 2011 December 12

Owocki 2006; Gal-Yam et al. 2014), By interaction with a binary companion (e.g. Podsiadlowski, Joss & Hsu 1992; Sana et al. 2012; Eldridge et al. 2013), or some combination of these two modes. If the envelope-stripping process is highly efficient, the helium shell is also removed before explosion, leading to the differentiation between SNe Ib (He-rich) and SNe Ic (He-poor). Hydrogen-poor CCSNe are generally referred to as stripped-envelope supernovae (SESNe).

SESNe are found to be observationally heterogeneous. For example, in some cases, the stripping process is incomplete and thus the envelope is left with some fraction of hydrogen. These SNe typically show H lines at early times that rapidly disappear after maximum light (Filippenko 1988; Filippenko, Matheson & Ho 1993), and their spectra resemble SNe Ib at late times. A small subset of SN Ib-like events show evidence of interaction with dense circumstellar material (CSM); having relatively narrow spectral emission lines (e.g. Foley et al. 2007; Pastorello et al. 2007; Hosseinzadeh et al. 2017), these objects have been dubbed SNe Ibn ('n' for 'narrow lines'). In addition, a subset of SNe Ic characterised by the presence broad spectral lines which indicate extremely high ejecta velocities ($\gtrsim 15\,000\,\mathrm{km\,s^{-1}}$) are designated as SNe Ic-BL (e.g. Modjaz et al. 2014). Objects within this subclass have been found to be associated with long-duration gamma-ray bursts (e.g. Woosley & Bloom 2006). Recently, a new class, SNe Icn, has been proposed by Gal-Yam et al. (2021) based on the prototype SN 2019hgp, followed by SNe 2021csp (Fraser et al. 2021; Perley et al. 2022) and 2021ckj (Pastorello et al. 2021). The early-time spectra of these objects are dominated by narrow lines with profiles similar to those seen in SNe Ibn, but originating from carbon and oxygen rather than He. In any case, all of the aforementioned SN classifications (Ib, IIb, Ibn, Ic, Ic-BL, and Icn) are, to some extent, related to the envelope of their progenitor star being stripped. Accordingly, we consider all of them to be SESNe in the analysis presented herein.

Owing to the efforts of various SN surveys spanning the globe, the study of SESNe with large light-curve samples has proliferated. Li et al. (2011) presented a set of roughly two dozen unfiltered SESN light curves within ∼60 Mpc. In the same year, Drout et al. (2011) presented *V*- and *R*-band light curves of 25 SESNe from the Palomar 60 inch telescope. Bianco et al. (2014) published multiband light curves of 64 SESNe obtained by the Harvard-Smithsonian Center for Astrophysics (CfA) SN group, and Taddia et al. (2015) presented expanded sets of multiband light curves of 20 SESNe from the Sloan Digital Sky Survey (SDSS) SN Survey II. In addition, Stritzinger et al. (2018a) published 34 SESN light curves from the first phase of the Carnegie Supernova Project (CSP-I). Despite these impressive efforts, the state of large-scale photometric studies of SESNe substantially lags that of other SNe (e.g. SNe Ia, which are routinely studied photometrically at the hundreds-of-objects scale).

Over the past two decades, our Lick Observatory Supernova Search (LOSS; Filippenko et al. 2001) program has invested considerably in both discovering and monitoring all kinds of SNe, including SESNe. Large light-curve samples have already been published by Ganeshalingam et al. (2010) and Stahl et al. (2019) for SNe Ia, and by de Jaeger et al. (2019) for SNe II. In this paper, we release the light curves of 70 SESNe observed by LOSS since 2003. In the remainder of the paper, we describe the sample (Section 2) and our data-reduction strategies (Section 3) before presenting an analysis of the light curves (Section 4) and offering our conclusions (Section 5).

2 DATA SAMPLE

The Berkeley SESN sample consists of 70 objects observed between 2003 and 2020. Two main telescopes were used for follow-up observations: (i) the fully robotic 0.76-m Katzman Automatic Imaging Telescope (KAIT; Filippenko et al. 2001), and (ii) the 1-m Anna Nickel telescope, both located at Lick Observatory on Mount Hamilton, near San Jose, CA, USA. Most SESNe in our sample were observed in multiple optical passbands (*B*, *V*, *R*, *I*), and some have additional *Clear*-band (unfiltered) data.[1] For a large fraction of SESNe in our sample, spectra were also obtained by our group using multiple facilities. A detailed analysis and release of the LOSS spectra of SESNe was published by Shivvers et al. (2019), so the present paper focuses exclusively on our photometric observations.

Table 1 provides the basic information for each SN in our sample, including its spectroscopic classification, host-galaxy name, distance, recession velocity, and Galactic extinction (Schlafly & Finkbeiner 2011). The listed classifications are adopted from the Transient Name Server[2] (TNS), but where they conflict with those given by Shivvers et al. (2019), we adopt the latter owing to the more sophisticated and systematic approach that resulted in their determinations. The single exception to this paradigm is SN 2008fz, which was classified as an SN Ic by Shivvers et al. (2019) but for which we adopt the classification of superluminous SN IIn (i.e. SLSN-IIn) from Drake et al. (2010). In summary, our SESN sample consists of 19 spectroscopically normal SNe Ib, 2 peculiar SNe Ib, six SNe Ibn, 14 normal SNe Ic, 1 peculiar SN Ic, 10 SNe Ic-BL, 15 SNe IIb, 1 ambiguous SN IIb/Ib/c, and 2 SLSNe.

The host-galaxy distances reported in Table 1 were obtained from the NASA/IPAC Extragalactic Database of redshift-independent distances (NED-D[3]) when available, and otherwise calculated using a standard cosmological model with $H_0 = 70\,\mathrm{km\,s^{-1}\,Mpc^{-1}}$, $\Omega_M = 0.30$, and $\Omega_\Lambda = 0.70$. Fig. 1 shows the redshift distribution of the 65 SESNe in our sample which have reliable host-galaxy heliocentric velocity measurements. The redshifts range from 0.0015 (SN 2011dh) to 0.0350 (SN 2009er), with an average value of 0.0136 and a standard deviation of 0.0082. In total, 40 SESNe have $z > 0.01$. For the remaining five SESNe without host heliocentric velocity measurements, we adopt redshifts from various literature sources (see the footnote of Table 1 for more details).

3 DATA REDUCTION

All photometric data published herein were obtained with the Lick KAIT and 1-m Nickel telescopes. Over the past two decades, the KAIT CCD and filter have been updated several times, resulting in four different CCD/filter combinations, which we refer as KAIT1-4 (see Ganeshalingam et al. 2010; Stahl et al. 2019 for more details). In its current configuration (KAIT4), KAIT is equipped with a Finger Lakes Instrument camera with 512 × 512 pixels covering a 6.7 × 6.7 $\mathrm{arcmin^2}$ field of view. The 1 -m Nickel is a human-operated telescope, but it can be remotely operated from the UC Berkeley campus. It is equipped with a thinned, Loral, 2048 × 2048 pixel CCD (binned by a factor of two along both axes to reduce the readout time), and has a 6.3 × 6.3 $\mathrm{arcmin^2}$ field of view. The filter set on the Nickel telescope was updated once, in 2009 March; we refer to the configuration before and after this change as Nickel1 and Nickel2, respectively (again, see Ganeshalingam et al. 2010; Stahl et al. 2019 for more details).

[1] A small fraction are covered with only *Clear*-band observations.
[2] www.wis-tns.org
[3] http://ned.ipac.caltech.edu/Library/Distances/

Table 1. SESN sample.

SN	Type	RA (h, m, s) (J2000)	Dec.(°,′,″) (J2000)	Discovery date (UT)	Host galaxy	A_V (MW)	Distance (Mpc)	Error (Mpc)	$V^a_{\rm helio}$ (host) (km s^{-1})	Error (km s^{-1})	Subtraction[b]?
2003gk	Ib	23:01:42.989	+02:16:08.69	2003-07-01	NGC 7460	0.24	48.2	28.0	3192	7	Y
2006el	IIb	22:47:38.50	+39:52:27.59	2006-08-25	UGC 12188	0.31	–	–	5115	14	Y
2006ep	Ib	00:41:24.88	+25:29:46.72	2006-08-30	NGC 214	0.10	51.1	12.3	4537	4	N
2006jc	Ibn	09:17:20.78	+41:54:32.69	2006-10-09	UGC 4904	0.06	–	–	1670	4	Y
2006lc	Ibn	22:44:24.45	−00:09:53.89	2006-10-21	NGC 7364	0.18	70.6	22.1	4865	5	Y
2007C	Ib	13:08:49.30	−06:47:01.00	2007-01-07	NGC 4981	0.12	22.7	3.1	1680	4	Y
2007D	Ic-BL	03:18:38.71	+37:36:26.39	2007-01-09	UGC 2653	0.92	103.8	5.6	6939	5	Y
2007ag	Ib	10:01:35.99	+21:36:42.01	2007-03-07	UGC 5392	0.08	114.8	1.7	6209	4	Y
2007cl	Ic	17:48:21.19	+54:09:05.18	2007-05-23	NGC 6479	0.12	–	–	6650	43	Y
2007kj	Ib	00:01:19.58	+13:06:30.60	2007-10-02	NGC 7803	0.22	–	–	5366	6	Y
2007ru	Ic-BL	23:07:23.14	+43:35:33.68	2007-11-27	UGC 12381	0.71	–	–	4636	6	N
2007rw	IIb	12:38:03.64	−02:15:40.10	2007-11-29	UGC 7798	0.09	–	–	2568	5	Y
2007rz	Ic	04:31:10.84	+07:37:51.49	2007-12-08	NGC 1590	0.55	–	–	3897	7	Y
2007uy	Ib-pec	09:09:35.35	+33:07:08.90	2007-12-31	NGC 2770	0.06	28.7	4.2	1947	2	Y
2008aq	IIb	12:50:30.42	−10:52:01.42	2008-02-27	MCG -02-33-20	0.12	32.0	3.0	2390	5	N
2008cw	IIb	16:32:38.27	+41:27:33.19	2008-06-01	SDSS J163238.15 + 412730.8	0.02	–	–	9726	25	Y
2008dq	Ic	16:06:03.11	+55:25:37.42	2008-06-25	UGC 10214	0.03	–	–	9401	15	Y
2008eb	Ib	18:11:52.17	+14:58:50.59	2008-07-07	NGC 6574	0.48	33.7	7.2	2282	5	Y
2008ew	Ic	16:58:28.92	+20:02:38.00	2008-08-10	IC 1236	0.22	38.0	–	6030	5	Y
2008fi	IIb	01:53:23.17	+ 29:21:28.40	2008-08-26	SDSS J015322.95 + 292131.2	0.17	–	–	–	–	N
2008fz	SLSN-IIn	23:16:16.60	+11:42:47.48	2008-09-22	Anon.	0.12	–	–	–	–	N
2008gj	Ic	22:36:28.57	+21:37:55.31	2008-10-19	NGC 7321	0.13	92.0	10.9	7145	5	Y
2009C	IIb	23:13:42.84	+49:40:47.21	2009-01-02	UGC 12433	0.79	–	–	6985	32	Y
2009K	IIb	04:36:36.77	−00:08:35.59	2009-01-14	NGC 1620	0.16	40.2	4.7	3512	1	Y
2009Z	IIb	14:01:53.61	−01:20:30.19	2009-02-02	SDSS J140153.80-012035.5	0.13	–	–	7534	3	N
2009er	Ib-pec	15:39:29.84	+24:26:05.32	2009-05-22	SDSS J153930.49 + 242614.8	0.12	–	–	10 492	67	N
2009gk	IIb	21:44:27.28	+14:53:57.30	2009-06-23	UGC 11803	0.24	–	–	7946	34	Y
2009hy	Ic	22:16:27.02	+16:28:13.01	2009-08-02	NGC 7244	0.14	–	–	7564	7	Y
2009jf	Ib	23:04:52.98	+12:19:59.48	2009-09-27	NGC 7479	0.31	28.3	6.1	2381	1	Y
2010cn	IIb	11:04:06.57	+04:49:58.69	2010-05-04	SDSS J110406.40 + 044955.5	0.13	–	–	7795	–	Y
2010gd	Ic	17:57:40.98	+27:49:48.11	2010-07-08	UGC 11064	0.16	107.1	21.6	7043	10	Y
2010hy	SLSN-I	18:59:32.89	+19:24:25.88	2010-09-04	Anon.	1.45	–	–	–	–	N
2011dh	IIb	13:30:05.12	+47:10:10.81	2011-06-01	NGC 5194	0.10	7.2	2.1	463	3	Y
2011fu	IIb	02:08:21.41	+41:29:12.30	2011-09-21	UGC 1626	0.21	–	–	5543	11	Y
2011gd	Ib	16:34:25.67	+21:32:28.39	2011-08-28	NGC 6186	0.13	–	–	2937	29	Y
2012aa	Ic	14:52:33.48	−03:31:54.01	2012-01-29	Anon.	0.28	–	–	–	–	Y
2012ap	Ic-BL	05:00:13.72	−03:20:51.22	2012-02-10	NGC 1729	0.14	39.3	3.3	3632	4	N

Table 1 – *continued*

SN	Type	RA (h, m, s) (J2000)	Dec.(°,′,″) (J2000)	Discovery date (UT)	Host galaxy	A_V (MW)	Distance (Mpc)	Error (Mpc)	$V^a_{\rm helio}$ (host) (km s^{-1})	Error (km s^{-1})	Subtraction[b]?
2012au	Ib	12:54:52.18	−10:14:50.21	2012-03-14	NGC 4790	0.13	22.9	2.8	1344	5	Y
2012fh	IIb/Ib/c	10:43:34.05	+24:53:29.00	2012-10-18	NGC 3344	0.09	11.9	6.2	580	1	Y
2013dk	Ic	12:01:52.72	−18:52:18.30	2013-06-22	NGC 4038	0.13	21.1	3.9	1642	12	Y
2014C	Ib	22:37:05.60	+34:24:31.90	2014-01-05	NGC 7331	0.25	13.4	2.7	816	1	Y
2014L	Ic	12:18:48.68	+14:24:43.49	2014-01-26	NGC 4254	0.11	15.2	2.0	2407	3	Y
2014as	Ic-BL	14:00:54.49	+40:58:59.59	2014-04-18	NGC 5410	0.04	–	–	3738	26	Y
2014cp	Ic-BL	02:25:30.46	−25:37:37.99	2014-06-23	ESO 479- G 001	0.05	45.1	7.2	4846	3	N
2014ds	IIb	08:11:16.45	+25:10:47.39	2014-10-11	NGC 2536	0.12	–	–	4118	17	Y
2014eh	Ic	20:25:03.86	−24:49:13.30	2014-11-03	NGC 6907	0.17	32.5	6.2	3182	4	N
2014ei	Ib	05:03:16.39	−02:56:11.00	2014-11-05	MCG -01-13-50	0.18	57.9	3.5	4329	4	Y
2015G	Ibn	20:37:25.58	+66:07:11.50	2015-03-23	NGC 6951	1.02	23.1	3.5	1424	1	Y
2015K	Ic	23:35:52.26	+23:36:52.09	2015-04-25	NGC 7712	0.15	49.0	3.2	3053	2	N
2015Q	Ib	11:47:35.081	+55:58:14.70	2015-06-17	NGC 3888	0.03	39.9	1.7	2408	11	Y
2015U	Ibn	07:28:53.87	+33:49:10.60	2015-02-13	NGC 2388	0.16	60.9	2.3	4134	5	Y
2015Y	Ib	09:02:37.87	+25:56:04.20	2015-04-11	NGC 2735	0.11	51.1	9.0	2450	5	Y
2015ap	Ib	02:05:13.32	+06:06:08.39	2015-09-08	IC1776	0.12	–	–	3410	5	Y
2016G	Ic-BL	03:03:57.74	+43:24:03.50	2016-01-09	NGC 1171	0.43	26.6	6.2	2742	6	Y
2016P	Ic-BL	13:57:31.10	+06:05:51.00	2016-01-19	NGC 5374	0.07	68.7	10.8	4382	7	Y
2016ajo	Ib	18:44:12.49	+24:09:29.70	2016-02-20	UGC 11344	0.34	58.5	4.2	3836	4	Y
2016bau	Ib	11:20:59.02	+53:10:25.60	2016-03-13	NGC 3631	0.04	10.3	5.4	1156	1	N
2016coi	Ic-BL	21:59:04.14	+18:11:10.46	2016-05-27	UGC 11868	0.23	17.2	–	1093	5	Y
2016gcm	Ic	21:04:55.22	+65:42:29.30	2016-09-08	PGC166705	1.33	–	–	7263	50	Y
2016gkg	IIb	01:34:14.46	−29:26:25.00	2016-09-20	NGC 613	0.05	20.9	5.7	1481	5	N
2016gqv	Ic-pec	04:02:48.53	+01:58:15.60	2016-09-28	UGC 02936	1.23	42.8	5.1	3813	7	Y
2016iyc	IIb	22:09:14.28	+21:31:17.51	2016-12-18	UGC 11924	0.21	–	–	3803	5	Y
2017ein	Ic	11:52:53.25	+44:07:26.20	2017-05-25	NGC 3938	0.06	12.7	7.8	809	4	N
2017iro	Ib	14:06:23.11	+50:43:20.20	2017-11-30	NGC 5480	0.05	24.2	6.0	1856	5	Y
2018cow	Ic-BL	16:16:00.22	+22:16:04.83	2018-06-16	CGCG 137-068	0.24	–	–	4241	39	N
2018ie	Ic-BL	10:54:01.06	−16:01:21.40	2018-01-18	NGC 3456	0.19	47.5	8.6	4267	7	N
2019wep	Ibn	11:04:37.033	+45:58:38.95	2019-12-07	UGC 06136	0.03	–	–	7521	11	N
2020nxt	Ibn	22:37:36.235	+35:00:07.68	2020-07-03	SDSS J223736.60 + 350007.4	0.21	–	–	–	–	Y
MOTJ120451.50 + 265946.6	Ib	12:04:51.50	+26:59:46.60	2014-10-28	NGC 4808	0.07	18.4	2.0	567	4	N
iPTF13bvn	Ib	15:00:00.152	+01:52:53.17	2013-06-16	NGC 5806	0.14	24.7	3.2	1359	5	Y

[a]For the five SNe without host heliocentric velocity measurements, redshifts are adopted as follows: $z_{\rm SN\ 2008fi} = 0.02600$ (Shivvers et al. 2019), $z_{\rm SN\ 2008fz} = 0.133$ (Drake et al. 2010), $z_{\rm SN\ 2010hy} = 0.19010$ (Shivvers et al. 2019), $z_{\rm SN\ 2012aa} = 0.07990$ (Shivvers et al. 2019), and $z_{\rm SN\ 2020nxt} \approx 0.02$ (Srivastav et al. 2020).
[b]Image subtraction is applied to remove host-galaxy contamination; see the text for details.

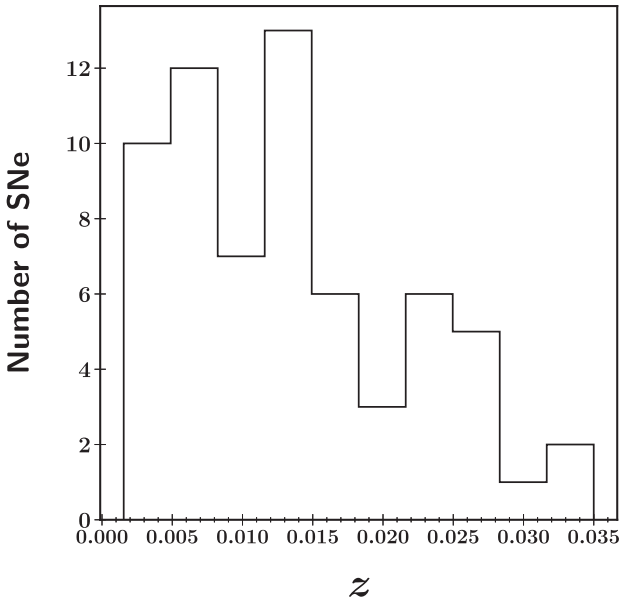

Figure 1. The redshift distribution of the 65 (out of 70 in total) SESNe in our sample which have reliable heliocentric velocity measurements from their host galaxies. The average redshift value is 0.0136 with a standard deviation of 0.0082, and 40 SESNe have $z > 0.01$.

A novel automated photometry pipeline[4] was developed by Stahl et al. (2019) to process the significant volume of SN observations produced by LOSS consistently and accurately, while at the same time requiring minimal human intervention. Although we defer the details to Stahl et al. (2019), we briefly summarise the main procedures here. All images are first treated to remove the bias level, and are then flat-fielded before being astrometrically calibrated using code provided by astrometry.net[5] (Lang et al. 2010). Where necessary, image subtraction is applied so as to remove host-galaxy contamination, with the template images being sourced on dark nights using the Nickel telescope after the SNe have faded beyond detection (generally >6 months after discovery). Point-spread-function (PSF) photometry is obtained using DAOPHOT (Stetson 1987) from the IDL Astronomy User's Library.[6] Nearby stars are chosen from the Pan-STARRS1[7] catalogue for calibration. Their magnitudes are first transformed into the Landolt system (Landolt 1983, 1992) using the empirical prescription (eq. 6) presented by Tonry et al. (2012), and then transformed to the appropriate KAIT/Nickel natural system (i.e. KAIT1-4 or Nickel1-2 as appropriate based on the equipment configuration on the date of observation). All apparent magnitudes are measured in the natural system, and the final results are then transformed to the standard system (see equation 1 a–d of Stahl et al. 2019) using local calibrators and the appropriate colour terms as given by Ganeshalingam et al. (2010) and Stahl et al. (2019). Note that when transforming from the natural system back to the standard system, there are additional errors associated with the transformation that are not accounted for owing to differences between the spectral energy distributions of SNe and the reference stars (e.g. Stritzinger et al. 2005).

[4]https://github.com/benstahl92/LOSSPhotPypeline
[5]https://astrometry.net
[6]http://idlastro.gsfc.nasa.gov/
[7]http://archive.stsci.edu/panstarrs/search.php

4 RESULTS

4.1 Photometry data release

We provide our final photometry in Tables 2 (standard system; see full Table S4 in the supplementary material) and 3 (natural system; see full Table S5 in the supplementary material) for all 70 SESNe in our sample. On average, each SN has 81 observations (median of 58) and 22 photometric points (median of 13 points) per filter, at a cadence of 3.6 d (median of 1.2 d). SN 2016coi has the best coverage (434 points), followed by SN 2015ap (351). The total number of distinct photometric observations published in this work is 5682. Of the 70 SNe in our sample, 38 have pre-maximum coverage and thus have their peak brightness measured in at least one band. Note that although several SNe in our sample have had their photometry previously published in individual papers, the magnitudes presented herein supersede these earlier measurements because (i) for some fields requiring image subtraction we have obtained new, higher quality templates, and (ii) better calibration sources are now available that were not used previously. Moreover, our processing is now significantly more systematic and self-consistent owing to our use of the battle-tested `LOSSPhotPypeline` (de Jaeger et al. 2019; Stahl et al. 2019; Stahl et al. 2020)

Note that in this release, we do not include the systematic uncertainty of 0.03 mag in *BVRI* that was determined and discussed in detail by Stahl et al. (2019). This amount of systematic uncertainty was estimated by investigating many factors that may contribute to the error, including evolution of colour terms, evolution of atmospheric terms, configurations between different telescopes, and galaxy-subtraction procedures. None of these factors contributed uncertainty over 0.03 mag, consistent with the estimate of Ganeshalingam et al. (2010). Though not included in our photometry tables (Table 2 and 3) or light-curve figures (e.g. Fig. 2 and Fig. S1 in the supplementary material, this uncertainty must be accounted for when combining our data set with others. Alongside the recent LOSS photometry release for SNe Ia (Stahl et al. 2019) and SNe II (de Jaeger et al. 2019), we aim for our SESN photometry to be used and further analysed by the astronomical community.

4.2 Light curves

Fig. 2 shows the apparent-magnitude light curves of all SESNe from our sample in the standard Landolt system without any extinction corrections applied. Note that we also include *Clear*-band light curves where available. Although unfiltered and thus non-standard, it is most similar to the *R* band (Li et al. 2003). The temporal axes are all in the observer frame and shifted such that times are measured relative to the times of maximum *V*-band brightness as determined by fitting the near-maximum data with low-order Legendre polynomials. In the 37 cases, where no maximum could be found via this method, the temporal axes are shifted relative to the time of the first observation. Such fitting was also applied to other bands if the data – after being supplemented with corresponding observations from Drout et al. (2011), Bianco et al. (2014), or Stritzinger et al. (2018a) – had sufficient near-maximum coverage.

4.3 Colour evolution and host extinction

Fig. 3 shows the $(B - V)$ (top left-hand panel) and $(V - R)$ (top right-hand panel) colour evolution of the SESNe in our sample which have the requisite observations in both bands, after correcting for Milky Way (MW) Galactic extinction (Schlafly & Finkbeiner 2011) but not

Table 2. Light-curve data in the standard system (only a portion of data is shown here as an example).

SN	MJD	*B* (mag)	*V* (mag)	*R* (mag)	*I* (mag)	*Clear* (mag)
2006el	53965.324	–	–	–	–	19.808 ± 0.464
2006el	53972.281	–	–	–	–	18.153 ± 0.250
2006el	53973.007	18.920 ± 0.069	18.335 ± 0.050	18.022 ± 0.095	17.846 ± 0.121	–
2006el	53973.304	–	–	–	–	17.952 ± 0.215
2006el	53973.977	18.782 ± 0.057	18.213 ± 0.048	17.922 ± 0.067	17.695 ± 0.091	–
2006el	53974.304	–	–	–	–	17.865 ± 0.175
2006el	53981.255	–	–	–	–	17.328 ± 0.140
2006el	53993.265	–	–	–	–	17.563 ± 0.215
2006el	53993.957	19.078 ± 0.093	18.118 ± 0.181	17.549 ± 0.296	17.367 ± 0.301	–
2006el	53994.925	19.316 ± 0.076	18.163 ± 0.059	17.668 ± 0.071	17.287 ± 0.084	–
2006el	54001.269	–	–	–	–	17.888 ± 0.183
2006el	54021.156	–	–	–	–	18.561 ± 0.462
2006el	54028.887	20.778 ± 0.143	19.548 ± 0.079	18.877 ± 0.063	18.171 ± 0.056	–
2006el	54030.193	–	–	–	–	18.679 ± 0.456
2006el	54039.155	–	–	–	–	18.772 ± 0.341
2006el	54047.126	–	–	–	–	18.751 ± 0.152
2006el	54058.109	–	–	–	–	18.828 ± 0.284
2006el	54071.111	–	–	–	–	18.917 ± 0.579

Table 3. Light-curve data in natural system (only a portion of data is shown here as example).

SN	MJD	*B* (mag)	*V* (mag)	*R* (mag)	*I* (mag)	*Clear* (mag)	System
2006el	53965.324	–	–	–	–	19.808 ± 0.464	kait3
2006el	53972.281	–	–	–	–	18.153 ± 0.250	kait3
2006el	53973.007	18.866 ± 0.068	18.366 ± 0.050	18.050 ± 0.086	17.825 ± 0.126	–	nickel1
2006el	53973.304	–	–	–	–	17.952 ± 0.215	kait3
2006el	53973.977	18.730 ± 0.056	18.243 ± 0.048	17.948 ± 0.061	17.672 ± 0.095	–	nickel1
2006el	53974.304	–	–	–	–	17.865 ± 0.175	kait3
2006el	53981.255	–	–	–	–	17.328 ± 0.140	kait3
2006el	53993.265	–	–	–	–	17.563 ± 0.215	kait3
2006el	53993.957	18.990 ± 0.089	18.169 ± 0.180	17.600 ± 0.269	17.334 ± 0.314	–	nickel1
2006el	53994.925	19.210 ± 0.074	18.224 ± 0.058	17.712 ± 0.064	17.248 ± 0.087	–	nickel1
2006el	54001.269	–	–	–	–	17.888 ± 0.183	kait3
2006el	54021.156	–	–	–	–	18.561 ± 0.462	kait3
2006el	54028.887	20.665 ± 0.141	19.613 ± 0.078	18.937 ± 0.056	18.110 ± 0.057	–	nickel1
2006el	54030.193	–	–	–	–	18.679 ± 0.456	kait3
2006el	54039.155	–	–	–	–	18.772 ± 0.341	kait3
2006el	54047.126	–	–	–	–	18.751 ± 0.152	kait3
2006el	54058.109	–	–	–	–	18.828 ± 0.284	kait3
2006el	54071.111	–	–	–	–	18.917 ± 0.579	kait3

host-galaxy extinction. Individually, we find that the colours trend blue at very early times (e.g. ∼10 d before *V*-band peak), and then become progressively more red until ∼20 d after *V*-band maximum. As a whole, however, the colours we observe span a wide range at nearly every epoch, in part because we have not (yet) performed any corrections for host extinction. As SESNe often reside in dusty star-forming regions (e.g. Van Dyk, Hamuy & Filippenko 1996; Kelly, Kirshner & Pahre 2008), it is likely that the extinction due to the galactic hosts of our SNe is generally the dominant component of the total line-of-sight extinction.

One useful way to estimate host extinction is to exploit its relationship with the equivalent width of Na I D absorption as measured from high-resolution spectra (e.g. Poznanski, Prochaska & Bloom 2012; Stritzinger et al. 2018b). Unfortunately, such data are difficult to obtain, and low-resolution spectra, though easier to procure, are usually not of sufficient quality for such measurements (Poznanski et al. 2011).

Distinct from spectral proxies using Na I D absorption, Drout et al. (2011) found that the $(V - R)$ colour evolution of SESNe has a small dispersion at ∼10 d after *V*-band peak, and thus can be exploited as a useful diagnostic for estimating host-galaxy extinction (Drout et al. 2011; Taddia et al. 2015; Stritzinger et al. 2018b). We therefore follow the approach of Drout et al. (2011) to estimate the extinction induced by the host galaxies of the SNe in our sample. To do this, we measure the $(V - R)$ colour at 10 d after *V*-band maximum, and apply extra extinction (assumed to be from the host) so that the $(V - R)$ colour reaches 0.26 mag – the mean $(V - R)$ colour found by Drout et al. (2011) after all corrections. We successfully applied this method to 31 SESNe in our sample with available data in both *V* and *R* at 10 d after *V*-band maximum. We note that a few SESNe in our measured sample have negative implied host-extinction values by doing this, but such values are sufficiently small to be consistent with no host extinction.

Fig. 4 shows a histogram of the estimated $E(B - V)$ values for the 31 SESNe in our sample (also listed in Table 4) assuming a Cardelli, Clayton & Mathis (1989) reddening law with $R_V = 3.1$. It clearly shows that SESNe usually suffer moderately-high extinction from their host galaxies, with a mean $E(B - V)$ value of 0.32 mag

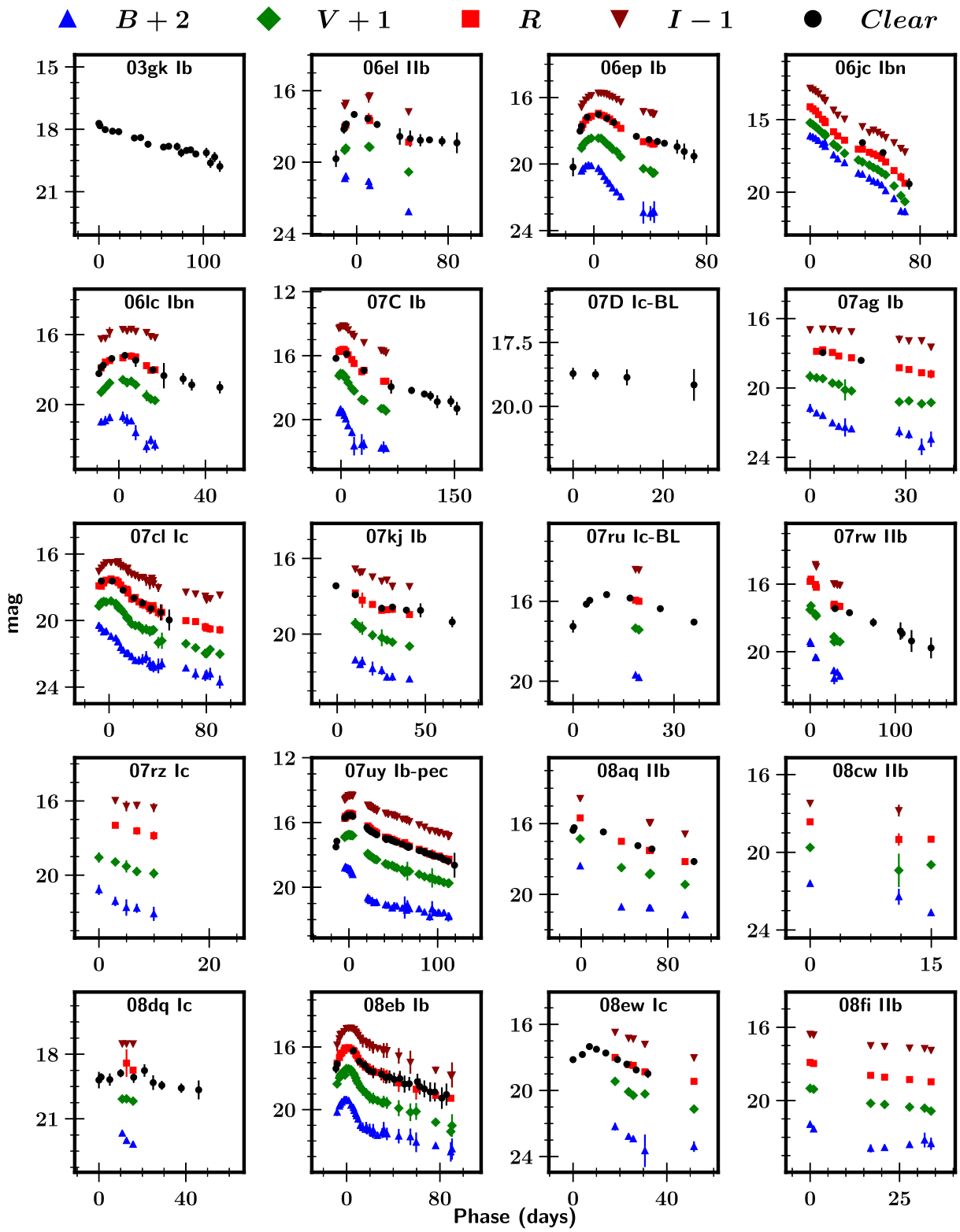

Figure 2. Apparent-magnitude light curves of the SESNe in our sample in the standard system (except for SN 2016P, which has data only in the natural system as shown in Fig. S1 in the supplementary material, without any corrections for extinction. Blue triangles are magnitudes in *B*, green diamonds are *V*, red squares are *R*, black circles are *Clear*, and dark-red inverted triangles are *I*. All dates have been shifted relative to the time of maximum *V*-band brightness if determined, and relative to the time of the first epoch otherwise. In each panel, the IAU name and the type are given.

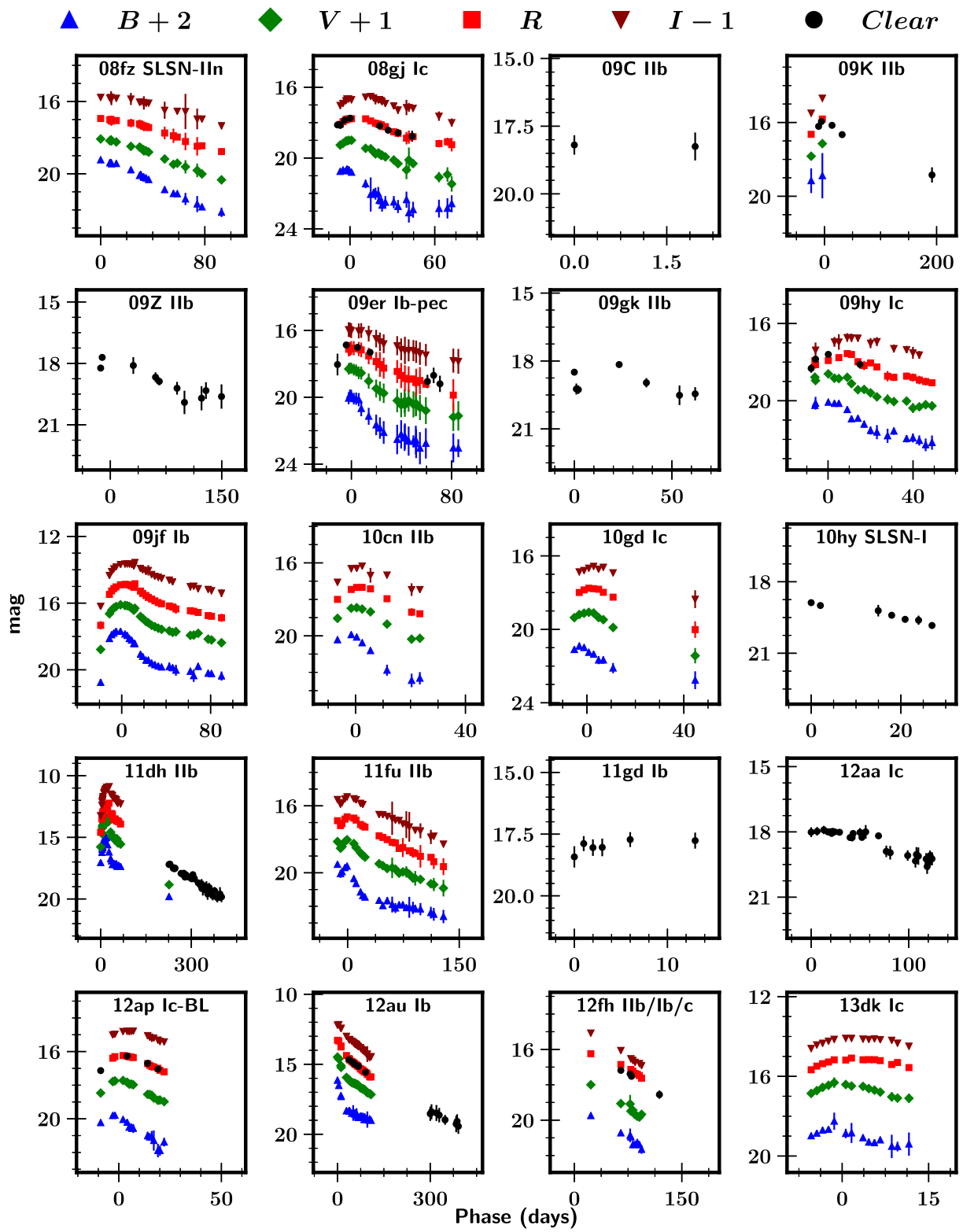

Figure 2 – *continued*

and standard deviation of 0.19 mag – consistent with the value found by other works using different SESN samples (Drout et al. 2011; Taddia et al. 2015; Stritzinger et al. 2018b). This mean host extinction is higher than recently studied samples of SNe Ia with mean $E(B-V) \approx 0.11$ mag (Burns et al. 2011; Stahl et al. 2019) and SNe II with mean $A_V \approx 0.9$ mag ($E(B-V) \approx 0.29$; Smartt et al. 2009).

After correcting for host extinction as described above, we plot the extinction-corrected $(B-V)$ (bottom left-hand panel) and $(V-R)$ (bottom right-hand panel) colour curves in Fig. 3. The scatter

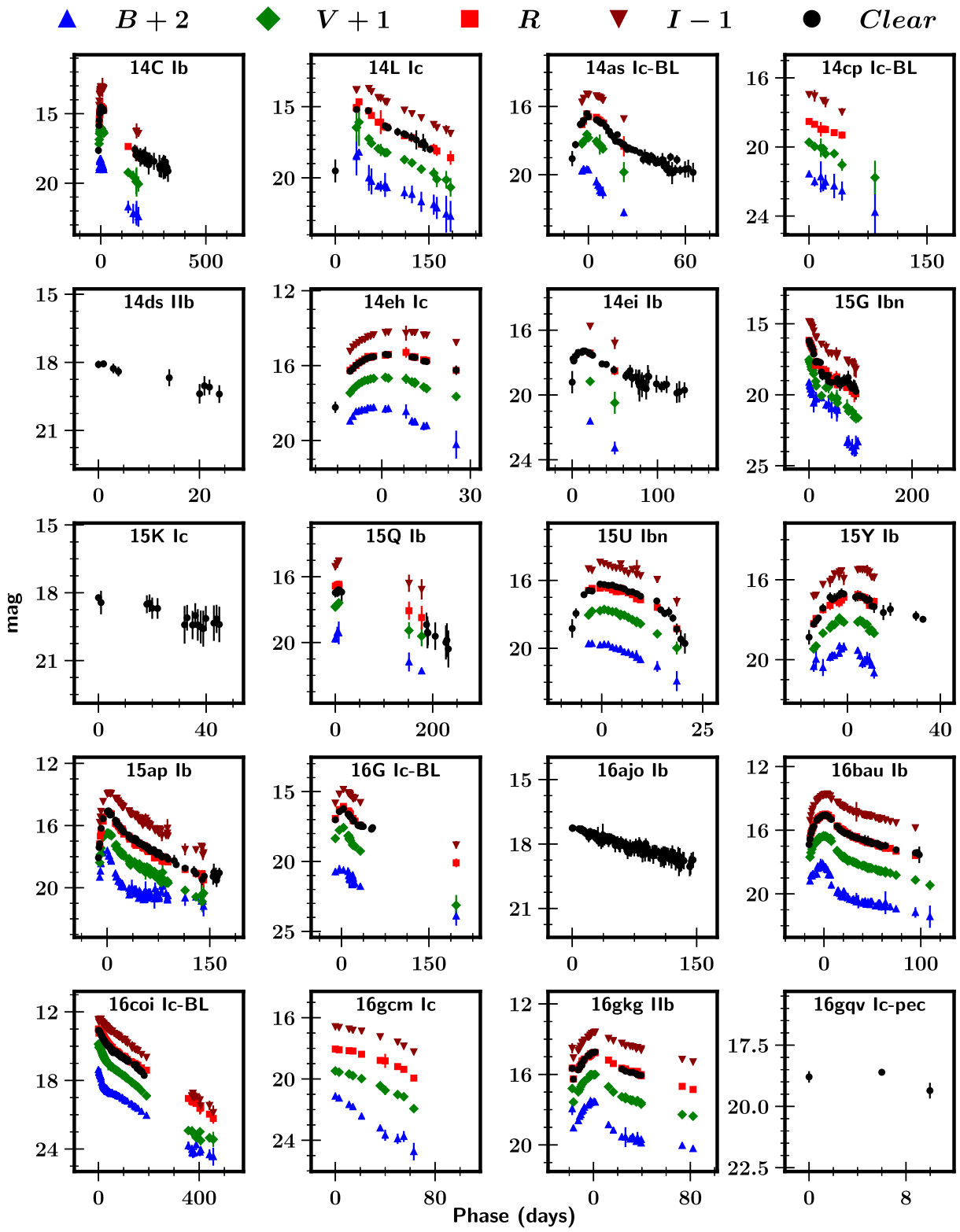

Figure 2 – *continued*

in $(V - R)$ colours is significantly decreased at 10 d after V-band maximum, consistent with the results of Drout et al. (2011), Taddia et al. (2015), and Stritzinger et al. (2018b). However, although its scatter is modestly reduced, the $(B - V)$ colour curve is by no means 'tight' like we observe for $(V - R)$. This is not surprising because the host extinction is estimated from the $(V - R)$ colour, not the $(B - V)$ colour as proposed by Drout et al. (2011). This indicates that the $(B - V)$ colour may not be as good a proxy as the $(V - R)$ colour, or that the host extinction is more complicated, e.g. the hosts of SESNe are known to be with a range of R_V (e.g. Stritzinger

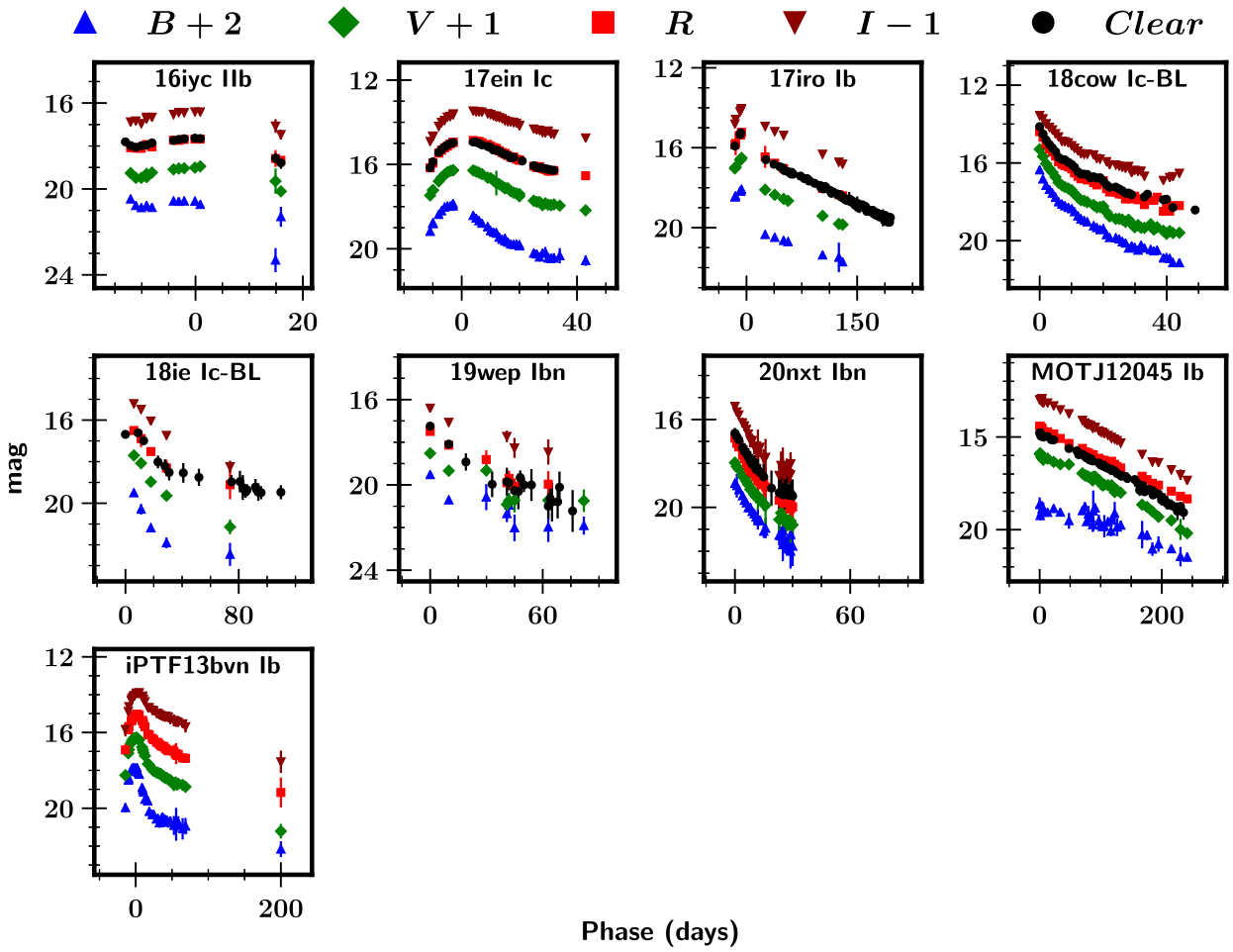

Figure 2 – *continued*

et al. 2018b), while adopting a constant $R_V = 3.1$ to derive $E(V - R)$ would lead to errors in $E(B - V)$ and more scatter. In either case, a better method for estimating the host-galaxy extinction for SESNe would be a valuable contribution to the field.

4.4 Absolute light curve and peak magnitude

Fig. 5 illustrates the absolute R-band light curves of the 31 SESNe in our sample for which we are able to fully correct for extinction (i.e. correct for both MW and host-galaxy effects). Overall, the SESNe show smooth light-curve shapes with ∼10–20 d rise times before maximum brightness (see Section 4.5 for more details), followed by a slow decay. A few Type IIb SESNe (e.g. SNe 2011fu, 2016iyc, 2016gkg) exhibit a decline dip at very early times (∼15 d before maximum) before rising. The early-time dips for these SNe IIb can be attributed to the shock-breakout cooling tail.

The peak R-band absolute magnitude of SESNe spans a wide range from −16 mag to over −19 mag. In order to compare the peak magnitudes between different subgroups, we plot the cumulative distribution of R-band absolute magnitude (after extinction correction) in Fig. 6. We find that our whole sample (29 SNe with both R peak and host-extinction measurements) has an average mean peak R absolute magnitude of -17.9 ± 0.7 mag. We also calculate the mean peak brightness for each subgroup and find a value for SNe Ib of -17.6 ± 0.7 mag (ten SNe), -17.9 ± 0.6 mag for seven SNe Ic, and -17.9 ± 1.0 mag for five SNe IIb. With admittedly small samples of three SNe Ic-BL and two SNe Ibn, we found -18.1 ± 0.3 and -18.4 ± 0.2 mag, respectively – brighter than the other subgroups (SNe Ib, Ic, IIb) and consistent with the conclusion reported by Taddia et al. (2015) that SNe Ic-BL are more luminous than both SNe Ib and SNe Ic, and that SNe Ic appear slightly brighter than SNe Ib. Our reported mean magnitudes are consistent with the results from Drout et al. (2011), who found -17.9 ± 0.9 mag for SNe Ib and -18.5 ± 0.8 mag for SNe Ic in the R band. Taddia et al. (2018) also reported similar trends, but in the r band, with -17.22 ± 0.60 mag, -17.66 ± 0.21 mag, and -17.45 ± 0.54 for SNe Ib, Ic, and IIb, respectively (see their table 5).

4.5 First-light time and rise time

With progressively more SESNe discovered and observed at very early phases, it has become possible to measure the true first-light time by fitting the observed light curve. Overall, the light-curve shape of SESNe resembles that of SNe Ia. Several empirical functions have been proposed to fit SESN light curves. For example, Taddia et al. (2015) used a phenomenological model – which was first employed by Bazin et al. (2011) for fitting SNe Ia – to fit their SESN light curves. Taddia et al. (2018) also proposed a three-component function that has proven to work well. Motivated by the former, we adopt a function proposed by Zheng & Filippenko (2017) for SN Ia light-curve fitting (Zheng, Kelly & Filippenko 2017) to fit the SESN light curves in our

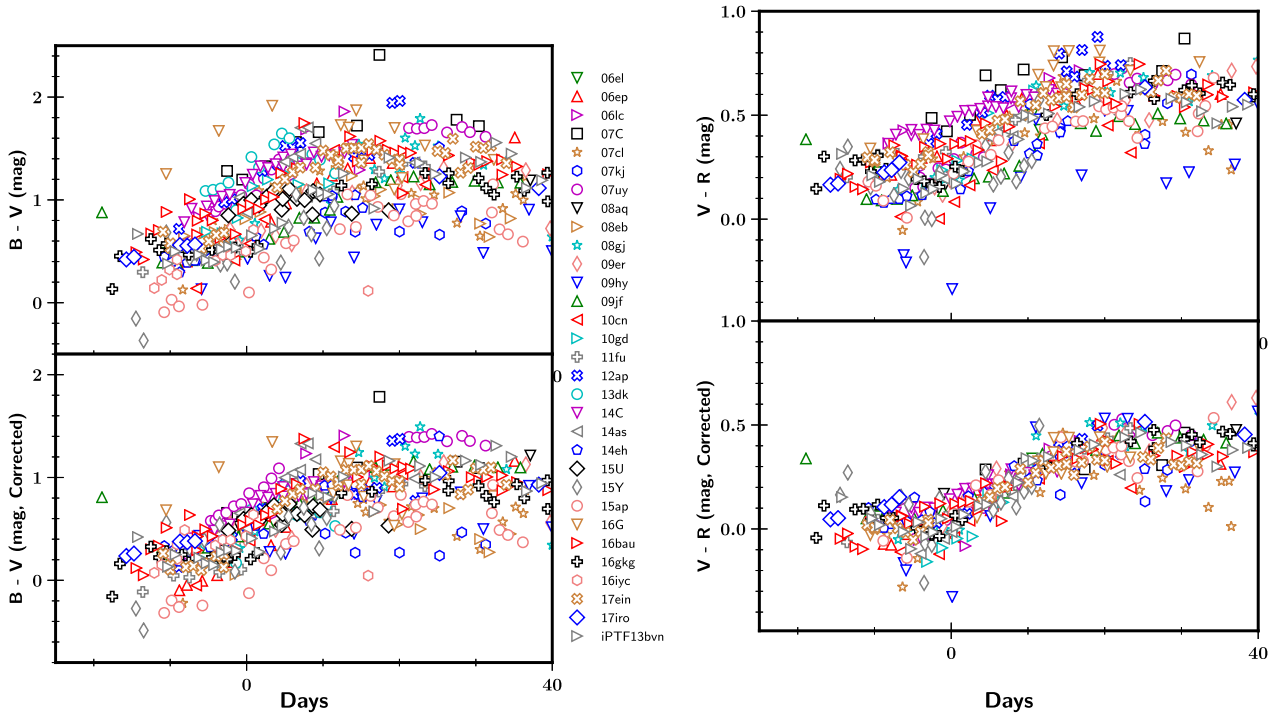

Figure 3. Left-hand panel: $(B - V)$ colour evolution of the SESNe in our sample having simultaneous observations in both bands, after correction for Galactic extinction (top panel), and with further correction for host extinction (bottom panel) using the empirical colour method (see the text for more details). Right-hand panel: similar to the left-hand panel, but for the $(V - R)$ colour.

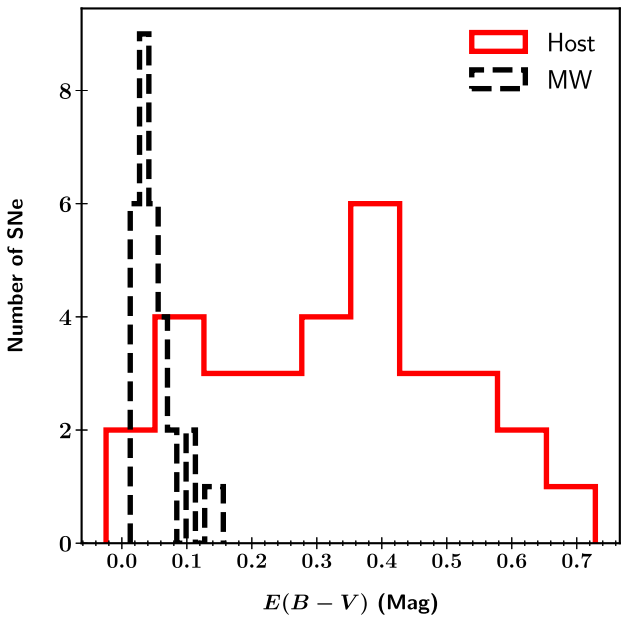

Figure 4. Distribution of host-galaxy extinction values for the 31 SESNe in our sample (solid red), revealing a mean $E(B - V)$ value of 0.32 mag with a standard deviation of 0.19 mag. The corresponding MW extinction is shown in dashed black.

sample. The function is given as

$$L = A' \left(\frac{t - t_0}{t_b}\right)^{\alpha_r} \left[1 + \left(\frac{t - t_0}{t_b}\right)^{s(\alpha_d)}\right]^{-2/s}, \quad (1)$$

where A' is a scaling constant, t_0 is the first-light time, t_b is the break time, α_r and α_d are the two power-law indices before and after the break, and s is a smoothing parameter. We have found that this function can provide satisfactory fits to the SESN light curves in our sample. Fig. 7 presents an example of this function fit to the well-observed SN Ib iPTF13bvn. This method directly takes the first-light time t_0 as a parameter in the fitting. Following the same procedure as Zheng et al. (2017), we fit for each filter with good-quality data. We finally adopt the mean value of the first-light time from the fitting if there are more than two measurements in different filters.

Using the estimated first-light time along with the peak time derived above (see Section 4.2), one can measure the rise time after correcting for the redshift. Table 5 gives the first-light time, peak time, and rise time for the SESNe in our sample. The rise times for different bands are calculated separately when different peak times are available. In addition, we collect the infrared peak time in the Y, J, H, and K_s filters for those SNe that are also presented by Bianco et al. (2014) or Taddia et al. (2018), in order to derive the rise time in infrared bands. Ten additional SESNe are added to the rise-time sample for this analysis; they are taken from the samples published by Drout et al. (2011), Bianco et al. (2014), Stritzinger et al. (2018a), and Taddia et al. (2018), and are listed at the bottom of Table 5.

Fig. 8 displays the rise time as a function of the effective wavelengths for different bands using all available fitting results for our sample. This figure is similar to fig. 10 of Taddia et al. (2015) and fig. 3 of Taddia et al. (2018). However, note that Taddia et al. (2015) use the explosion time – defined as the average between the epochs of last non-detection and first detection – instead of the first-light time, and Taddia et al. (2018) use the offset of peak time in different filters relative to the r-band peak time in their Fig. 10. Consequently, we claim that the first-light times and rise times presented herein are the first true measurements of such for a large sample of SESNe. Also for the first time, we measure accurate rise times of a large sample

Table 4. Light-curve properties.

SN	Type	z	$E(B-V)_{\rm host}$	$M_{\rm max}(R)$	$m_{\rm max}(U)$	$m_{\rm max}(B)$	$m_{\rm max}(g)$	$m_{\rm max}(V)$	$m_{\rm max}(R)$	$m_{\rm max}(r)$	$m_{\rm max}$(clear)	$m_{\rm max}(I)$	$m_{\rm max}(i)$
2006el	IIb	0.017 062	0.25	−17.88	–	18.28	–	17.60	17.33	–	–	–	17.44
2006ep	Ib	0.015 134	0.45	−17.73	18.57	17.97	17.65	17.39	16.98	17.19	–	16.72	17.05
2006lc	Ibn	0.016 228	0.45	−18.26	19.79	18.51	18.09	17.67	17.23	17.32	–	16.71	17.22
2007C	Ib	0.005 604	0.62	−17.82	–	17.28	–	16.13	15.58	15.76	–	15.13	15.50
2007cl	Ic	0.022 182	0.35	−18.27	–	–	–	17.85	17.60	17.48	–	17.42	17.69
2007kj	Ib	0.017 899	0.42	–	18.30	17.92	17.74	17.66	–	17.56	–	–	17.62
2007ru	Ic-BL	0.015 464	–	–	–	–	–	–	–	–	15.63	–	–
2007uy	Ib-pec	0.006 494	0.30	−17.62	–	16.72	–	15.76	15.46	15.57	–	15.30	15.63
2008aq	IIb	0.007 972	−0.02	–	–	16.40	–	15.84	–	–	–	–	15.95
2008eb	Ib	0.007 612	0.37	−17.89	–	17.36	–	16.39	16.03	–	–	15.76	–
2008ew	Ic	0.020 114	–	–	–	–	–	–	–	–	17.51	–	–
2008gj	Ic	0.023 833	0.30	−17.94	–	18.64	–	18.01	17.71	–	–	17.47	–
2009K	IIb	0.011 715	–	–	17.46	16.64	16.36	16.08	–	15.83	–	–	–
2009Z	IIb	0.025 131	–	–	18.36	17.75	17.48	17.25	–	17.16	–	–	17.16
2009er	Ib-pec	0.034 998	0.16	−19.38	–	17.92	–	17.24	17.05	17.17	–	–	17.25
2009gk	IIb	0.026 505	–	–	–	–	–	–	–	–	18.05	–	–
2009hy	Ic	0.025 231	−0.01	−17.63	–	18.02	–	17.68	17.66	–	–	17.77	–
2009jf	Ib	0.007 942	0.07	−17.81	–	15.66	–	15.07	14.86	14.99	–	14.63	15.00
2010cn	IIb	0.026 001	0.19	−18.51	–	17.90	–	17.46	17.33	–	–	17.19	–
2010gd	Ic	0.023 493	0.50	−18.75	–	18.91	–	18.09	17.76	–	–	17.62	–
2011fu	IIb	0.018 489	0.41	−19.02	–	17.66	–	17.06	16.67	–	–	16.49	–
2012ap	Ic-BL	0.012 115	0.59	−18.29	–	17.79	–	16.71	16.23	–	–	15.78	–
2013dk	Ic	0.005 477	0.73	−18.38	–	16.65	–	15.37	15.12	–	–	15.07	–
2014C	Ib	0.002 722	0.50	−17.55	–	16.25	–	15.05	14.52	–	14.57	14.07	–
2014L	Ic	0.008 029	–	–	–	–	–	–	–	–	–	–	–
2014as	Ic-BL	0.012 469	0.37	−18.09	–	17.63	–	16.78	16.51	–	16.47	16.26	–
2014eh	Ic	0.010 614	0.11	−17.57	–	16.23	–	15.63	15.40	–	15.41	15.17	–
2014ei	Ib	0.014 440	–	–	–	–	–	–	–	–	17.30	–	–
2015U	Ibn	0.013 790	0.36	−18.51	–	17.73	–	16.74	16.43	–	16.23	16.01	–
2015Y	Ib	0.008 172	0.12	−17.14	–	17.27	–	16.84	16.78	–	16.66	16.41	–
2015ap	Ib	0.011 375	0.22	−18.92	–	15.53	–	15.45	15.18	–	15.09	14.89	–
2016G	Ic-BL	0.009 146	0.57	−17.79	–	18.58	–	16.56	16.07	–	16.26	15.86	–
2016bau	Ib	0.003 856	0.37	−15.99	–	16.20	–	15.36	15.02	–	15.05	14.75	–
2016gkg	IIb	0.004 940	0.29	−17.56	–	15.58	–	14.99	14.79	–	14.78	14.68	–
2016iyc	IIb	0.012 685	0.07	−16.36	–	18.55	–	17.99	17.68	–	17.65	17.41	–
2017ein	Ic	0.002 699	0.43	−16.79	–	15.91	–	15.19	14.82	–	14.87	14.45	–
2017iro	Ib	0.006 191	0.18	−17.54	–	16.07	–	15.39	14.87	–	14.98	14.79	–
iPTF13bvn	Ib	0.004 533	0.25	−17.65	–	15.86	–	15.26	15.03	–	–	14.90	–

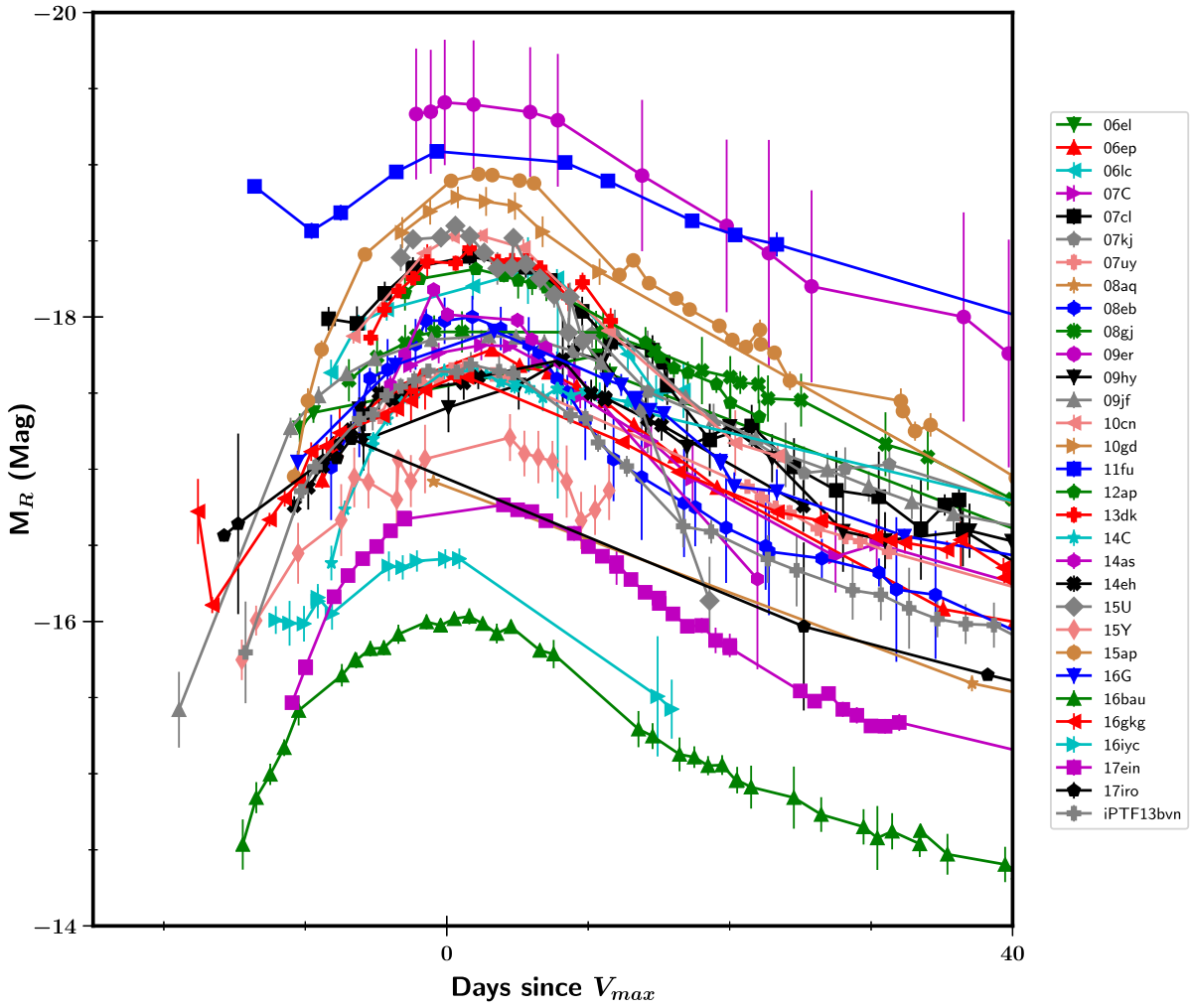

Figure 5. Absolute *R*-band light curves of the 31 SESNe in our sample that can be fully extinction corrected, only photometric error, not distance or host-extinction error, was included in this plot. SESNe show smooth light-curve shapes, with ∼10–20 d rise times, followed by a slow post-maximum decay. A few Type IIb SESNe show a decline dip at very early times, which can be attributed to the shock-breakout cooling tail.

of SESNe in infrared bands. These measurements are important for understanding the explosion properties of SESNe (see Section 4.6).

As can be seen in Fig. 8, the rise time is generally longer in red filters than it is in blue filters, confirming the similar result found by Bianco et al. (2014), Taddia et al. (2015, 2018). The rise time in infrared bands is typically a factor of ∼1.5 longer than in blue bands (*U* or *B*). The rise times in different subtypes of SNe also show differences, which we visualize via the cumulative distribution of the rise time for each subgroup consisting of SNe Ib, Ic, and IIb in Fig. 9. A Kolmogorov–Smirnov (K-S) test comparing SNe Ib and SNe Ic in the *B* band gives a *p*-value of 0.013, showing a significant difference between the two populations, and an analogous K-S test between SNe IIb and SNe Ib in the *B* band gives a *p*-value of 0.025 – also showing a significant difference between the two populations. We find that the average rise time for SNe IIb, Ib, and Ic are 23.5, 19.9, and 13.8 d (respectively) in the *B* band, and 26.1, 22.6, and 19.2 d (respectively) in the *R* band. It is obvious that for almost all bands, SNe IIb have the longest rise times, while SNe Ic have the shortest, consistent with the findings of Valenti et al. (2011) and Taddia et al. (2015, 2018). We also notice that the different rise times between each SN subtype are less clear in infrared bands compared to optical bands, though we caution that the infrared sample is much smaller.

The bottom row in Fig. 9 shows the difference between rise times in the selected two bands. Typically, SNe Ic take more time for redder bands to reach peak after *B*-band peak compared with SNe IIb, opposite to the aforementioned rise-time relations.

4.6 Light-curve fitting and modelling

To further study the physical properties of the SESNe in our sample, we model the multiband light curves using the ^{56}Ni model subject to the following assumptions: (i) the bolometric luminosities of the photospheres of the SNe are powered by ^{56}Ni cascade decay (Arnett 1982; Chatzopoulos, Wheeler & Vinko 2012; Wang et al. 2015), (ii) the spectral energy distributions of the SNe can be described by the blackbody or ultraviolet-absorbed blackbody function (see Nicholl, Guillochon & Berger 2017, and references therein), and (iii) the velocities of the SN photospheres are constant at early times, and the radii of the photospheres are determined by the bolometric luminosities and the temperature at the late epochs when the temperature no longer changes (see, e.g. equations 8 and 9 of

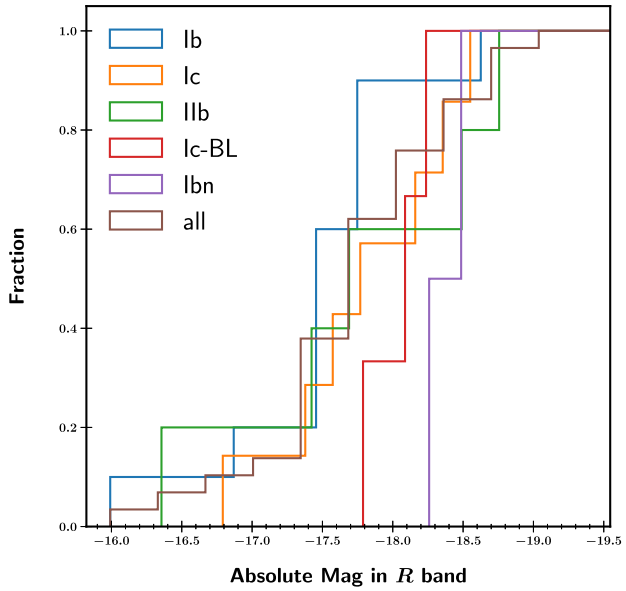

Figure 6. Cumulative distribution of the absolute *R*-band peak magnitudes of the 31 SESNe in our extinction-corrected sample. SESNe show a wide range from −16 mag to brighter than −19 mag. SNe Ic-BL and SNe Ibn appear, on average, to be more luminous than both SNe Ib and SNe Ic, and SNe Ic seem to be slightly brighter than SNe Ib.

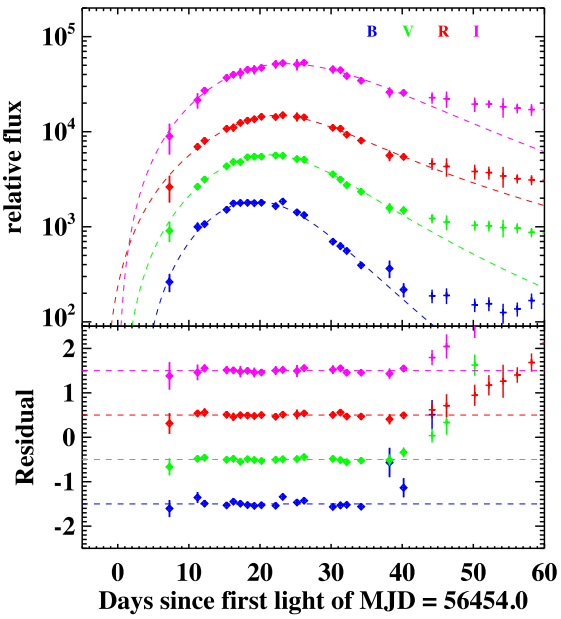

Figure 7. An example of multiband light-curve fitting to the well-observed SN iPTF13bvn using the function (see the text) proposed by Zheng & Filippenko (2017), which was originally used for fitting SN Ia light curves. 'Diamond' data points are included in the fitting while 'cross' data points are not. This example demonstrates that the same function can also be used for fitting SESN light curves.

Nicholl et al. 2017). We do not consider the case of interactions with dense CSM, which usually make the light curves flattened at late times and are more likely related to Type IIn SNe, while the light curves in our sample do not show enough evidence for such cases. The definitions, units, and prior ranges of the free parameters of the ^{56}Ni model are given in Table 6, where the prior is uniformly sampled either linearly or in log space over the range. We employ a Markov chain Monte Carlo method via the `emcee` Python package (Foreman-Mackey et al. 2013) to get the best-fitting parameters and 3σ confidence ranges of the fitted parameters.

The ^{56}Ni model-fitting results for all SESNe in our sample are shown in Fig. S2 in the supplementary material, except SN 2009C for which there is not enough data to meaningfully constrain the fitting. The best-fitted parameter values are given in Table S1 in the supplementary material, where we also list in parentheses the median values for comparison. As one can see, for most of the SNe, though the *B*-band fitting deviates more than other filters for some cases, our ^{56}Ni model can fit the general observed light curves with reasonable physical parameters.

However, for a group of SNe with double peaks or rebrightening after initial fading (including SNe 2011fu, 2015Y, 2016gkg, and 2016iyc), our simple ^{56}Ni model fails to adequately fit the early-time initial decay. In these cases, we therefore adopt an additional cooling component and refit the light curve. The new cooling plus ^{56}Ni model contains three additional parameters: (i) the mass of the extended envelope ($M_{\rm e}$), (ii) the radius of the extended envelope ($R_{\rm e,\,12}$), and (iii) the energy passed into the extended envelope ($E_{\rm e,\,50}$) from the SN core (Piro, Haynie & Yao 2021). The cooling plus ^{56}Ni model can better fit the light curves as shown in Fig. S3 in the supplementary material and the new fitting results are given in Table S2 in the supplementary material.

For another group of four SNe (including SNe 2008fz, 2010hy, 2012aa, and 2018cow), the ^{56}Ni model results suggest extremely high ^{56}Ni masses, some even higher than the ejecta mass, which is clearly unphysical. For these four luminous or superluminous SNe, we therefore adopt the magnetar model (Kasen & Bildsten 2010; Woosley 2010; Chatzopoulos et al. 2012; Wang et al. 2015; Dai et al. 2016) to refit the light curves. Three new parameters are included compared to the ^{56}Ni model (also listed in Table S1 in the supplementary material): the initial period (P_0), the magnetic field strength of the magnetar ($B_{\rm p,\,14}$), and the gamma-ray opacity of magnetar photons ($\kappa_{\gamma,\,\rm mag}$). The magnetar model fitting is shown in Fig. S4 in the supplementary material. and the results are given in Table S3 in the supplementary material. Compared to the ^{56}Ni model, the magnetar model provides comparable fitting results for the light curves, but with more reasonable physical parameters, indicating that a small fraction of SESNe may be powered by central magnetars.[8]

To summarize, Fig. 10 shows the cumulative distribution of the four parameters ($M_{\rm ej}$, v_9, $M_{\rm Ni}$, and $T_{\rm f}$) from the model fitting. We find that SNe Ic tend to have lower ejecta masses and also slower ejecta velocities, on average, compared to SNe Ib and SNe IIb. On the other hand, the ^{56}Ni mass of SNe Ic tends to be higher than in SNe Ib and SNe IIb, consistent with the findings Of Prentice et al. (2016) (see table 10 in the paper). Anderson (2019) reached a similar conclusion (see table 1 in their paper) that SNe Ic have higher ^{56}Ni mass than SNe IIb, though their estimate of the ^{56}Ni mass for SNe Ib is comparable to that of SNe Ic. The temperature floor of the photosphere distribution shows no significant difference between different subtypes.

5 CONCLUSION

In this paper, we have presented multiband (*BVRI*, along with some *Clear*) light curves of a large sample of SESNe observed by the KAIT and Nickel telescopes at Lick Observatory under the LOSS

[8]Note that we cannot exclude the possibility of a hidden (fainter) magnetar in other SESNe, but those SESNe do not require the fainter magnetar in the model fitting.

Table 5. Rise-time information.

SN	Type	z	t_0 (MJD)	$t_r(u)$	$t_r(B)$	$t_r(g)$	$t_r(V)$	$t_r(R)$	$t_r(r)$	$t_r(Clear)$	$t_r(I)$	$t_r(i)$	$t_r(Y)$	$t_r(J)$	$t_r(H)$	$t_r(K)$
2006el	IIb	0.017 062	53 958.0 ± 1.2	–	24.5 ± 3.8	–	25.0 ± 2.5	25.0 ± 5.6	–	–	–	28.5 ± 1.5	–	–	–	–
2006ep	Ib	0.015 134	53 964.7 ± 2.4	17.7 ± 3.0	19.8 ± 2.4	20.4 ± 3.0	22.2 ± 2.6	24.3 ± 3.0	24.0 ± 2.8	–	25.8 ± 2.5	25.8 ± 2.4	28.7 ± 2.4	30.2 ± 2.4	30.4 ± 2.4	–
2006lc	Ibn	0.016 228	54 022.0 ± 0.9	17.0 ± 3.6	18.3 ± 2.1	18.3 ± 3.6	19.1 ± 2.1	21.8 ± 1.6	20.5 ± 2.0	–	22.7 ± 1.1	21.4 ± 1.1	25.2 ± 1.6	26.2 ± 1.6	26.4 ± 1.6	–
2007ru	Ic-BL	0.015 464	54 426.5 ± 2.1	–	–	–	–	–	–	13.8 ± 3.2	–	–	–	–	–	–
2007uy	Ib-pec	0.006 494	54 458.0 ± 1.0	–	19.2 ± 1.1	–	23.0 ± 1.1	25.3 ± 1.1	25.5 ± 1.1	–	26.1 ± 1.1	26.1 ± 1.1	–	31.9 ± 1.0	33.1 ± 1.0	34.2 ± 1.0
2008eb	Ib	0.007 612	54 645.4 ± 0.9	–	17.0 ± 1.0	–	18.0 ± 1.1	18.7 ± 1.1	–	–	19.7 ± 1.1	–	–	–	–	–
2009K	IIb	0.011 715	54 838.3 ± 1.6	26.4 ± 3.2	28.2 ± 1.9	28.9 ± 1.9	31.0 ± 1.7	–	32.9 ± 1.7	–	–	–	38.3 ± 1.6	37.9 ± 1.6	41.9 ± 1.6	–
2009jf	Ib	0.007 942	55,097.8 ± 1.1	–	21.0 ± 1.5	–	23.3 ± 1.3	25.3 ± 1.8	25.5 ± 1.5	–	26.5 ± 1.3	26.8 ± 1.8	–	31.1 ± 1.1	32.3 ± 1.1	35.0 ± 1.1
iPTF13bvn	Ib	0.004 533	56 454.0 ± 1.4	–	19.5 ± 1.5	–	21.4 ± 1.6	22.8 ± 1.5	–	–	24.0 ± 1.6	–	–	–	–	–
2014C	Ib	0.002 722	56 656.6 ± 0.8	–	11.1 ± 0.9	–	13.7 ± 0.9	14.8 ± 0.9	–	14.4 ± 1.4	15.9 ± 0.9	–	–	–	–	–
2014as	Ic-BL	0.012 469	56 758.9 ± 1.1	–	10.5 ± 1.3	–	12.3 ± 1.2	13.3 ± 2.1	–	13.1 ± 2.1	13.5 ± 2.1	–	–	–	–	–
2014eh	Ic	0.010 614	56 955.1 ± 1.0	–	16.9 ± 1.7	–	19.6 ± 1.7	21.9 ± 2.3	–	22.0 ± 2.9	24.4 ± 2.3	–	–	–	–	–
2014ei	Ib	0.014 440	56 960.5 ± 2.3	–	–	–	–	–	–	17.9 ± 2.4	–	–	–	–	–	–
2015U	Ibn	0.013 790	57 061.0 ± 0.9	–	7.6 ± 1.1	–	9.5 ± 1.0	9.7 ± 1.0	–	9.9 ± 1.0	9.8 ± 1.0	–	–	–	–	–
2015Y	Ib	0.008 172	57 113.6 ± 2.2	–	23.3 ± 3.0	–	23.9 ± 3.0	25.5 ± 3.0	–	23.9 ± 2.8	26.6 ± 3.0	–	–	–	–	–
2015ap	Ib	0.011 375	57 270.1 ± 0.9	–	12.2 ± 2.4	–	14.9 ± 2.4	16.6 ± 1.1	–	15.3 ± 1.0	18.0 ± 1.0	–	–	–	–	–
2016bau	Ib	0.003 856	57 452.4 ± 1.0	–	22.1 ± 1.2	–	25.3 ± 1.1	25.5 ± 1.1	–	25.7 ± 1.1	27.0 ± 1.1	–	–	–	–	–
2016gkg	IIb	0.004 940	57 644.4 ± 0.8	–	24.9 ± 1.1	–	26.4 ± 1.1	27.3 ± 0.9	–	28.1 ± 4.0	28.3 ± 4.0	–	–	–	–	–
2017ein	Ic	0.002 699	57 895.7 ± 0.8	–	14.8 ± 2.6	–	17.5 ± 2.6	19.0 ± 2.6	–	18.1 ± 2.6	20.1 ± 2.6	–	–	–	–	–
Literature sample.																
2004dk	Ib	0.005 247	53 213.9 ± 0.7	–	–	–	24.7 ± 1.9	27.7 ± 1.9	–	–	–	–	–	–	–	–
2004ex	IIb	0.017 549	53 281.7 ± 1.0	22.9 ± 1.7	23.9 ± 1.7	24.3 ± 1.7	25.4 ± 1.1	–	26.5 ± 1.1	–	–	28.4 ± 1.1	32.1 ± 1.0	27.5 ± 1.0	30.3 ± 1.0	–
2004fe	Ic	0.017 896	53 302.6 ± 1.2	11.9 ± 1.3	13.3 ± 1.6	13.9 ± 2.1	15.1 ± 1.6	16.7 ± 1.7	16.6 ± 1.4	–	–	18.0 ± 1.3	–	–	–	–
2004gv	Ib	0.019 927	53 343.9 ± 0.9	19.2 ± 1.1	20.6 ± 1.1	20.6 ± 1.1	21.9 ± 1.6	–	23.7 ± 1.6	–	–	25.7 ± 1.4	26.9 ± 0.9	26.8 ± 0.9	32.1 ± 0.9	–
2005hg	Ib	0.021 308	53 659.4 ± 3.2	19.9 ± 3.2	21.5 ± 3.2	–	23.1 ± 3.2	25.0 ± 3.4	25.1 ± 3.2	–	–	27.3 ± 3.2	–	32.3 ± 3.2	33.6 ± 3.2	35.8 ± 3.2
2006T	IIb	0.008 092	53 762.7 ± 1.1	15.5 ± 1.5	16.3 ± 1.2	16.6 ± 1.5	17.7 ± 1.3	–	18.5 ± 1.3	–	–	19.8 ± 1.3	20.7 ± 1.1	21.6 ± 1.1	23.8 ± 2.0	–
2007Y	Ib	0.004 637	54 142.4 ± 2.0	18.9 ± 2.1	19.9 ± 2.1	20.5 ± 2.1	21.9 ± 2.1	–	23.3 ± 2.1	–	–	24.1 ± 2.3	23.3 ± 2.0	25.2 ± 2.0	24.5 ± 2.3	–
2008D	Ib	0.006 494	54 468.9 ± 0.9	–	22.2 ± 3.7	–	23.9 ± 3.3	–	24.7 ± 3.7	–	–	25.5 ± 1.0	–	–	–	–
2009bb	Ic	0.009 877	54 909.6 ± 1.0	9.1 ± 1.4	10.3 ± 1.4	11.5 ± 2.7	12.9 ± 2.7	–	13.9 ± 2.7	–	–	14.9 ± 2.7	20.2 ± 1.0	18.5 ± 1.0	17.5 ± 1.0	–
2009iz	Ib	0.014 196	55,077.3 ± 1.1	–	28.2 ± 1.2	–	31.0 ± 2.8	–	33.1 ± 2.8	–	–	36.3 ± 1.3	–	42.9 ± 1.1	47.1 ± 1.1	45.3 ± 1.1

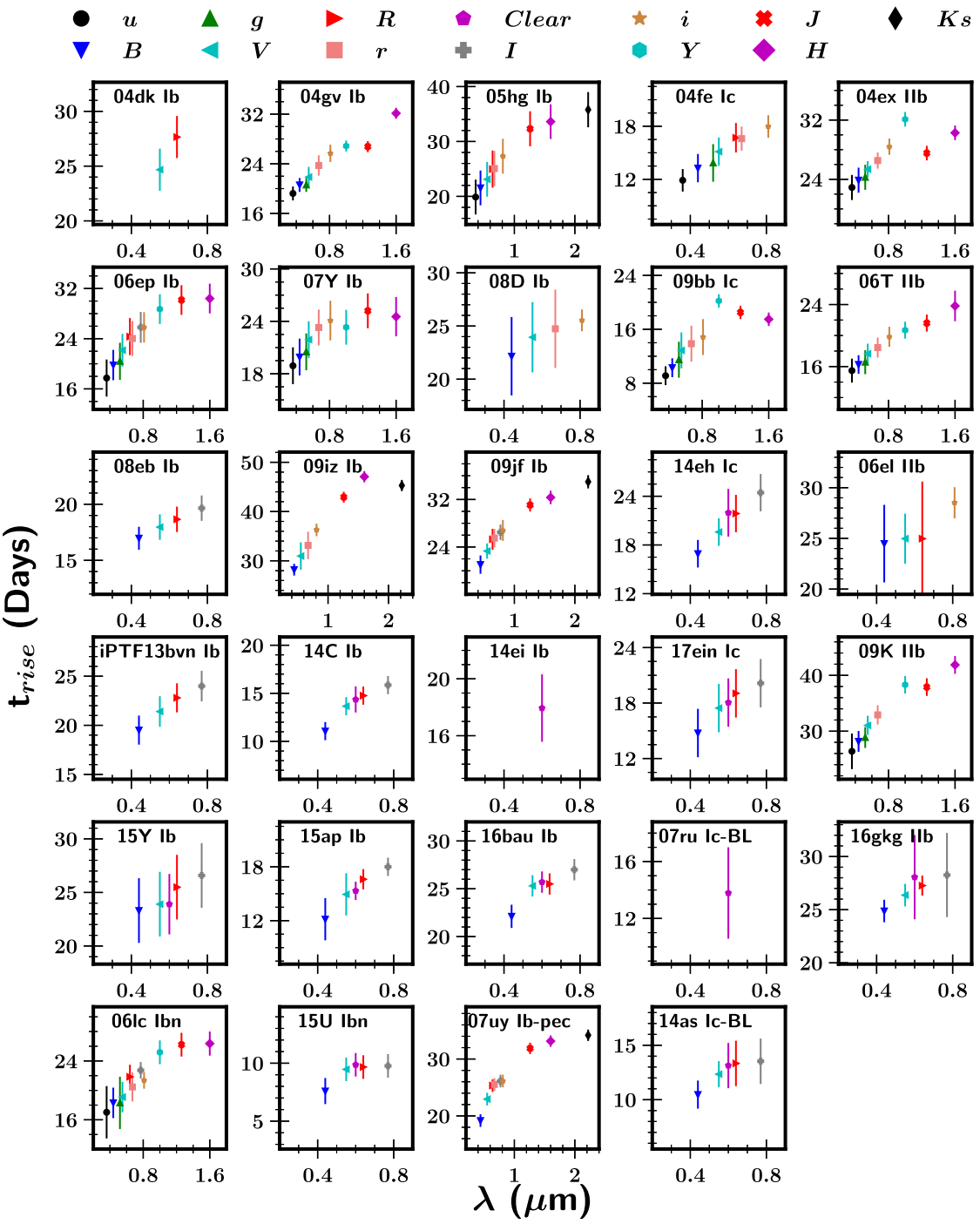

Figure 8. Rise time derived from 29 SESNe as a function of the effective wavelengths for different bands, colour coded as shown in the top legend. The rise time is generally longer in redder filters than it is in bluer filters. The rise time in infrared bands is typically a factor of ∼1.5 longer than in blue bands (*U* or *B*).

follow-up program from 2003 through 2020. Our data are processed in a homogeneous fashion, and here we publicly release all derived data products to the supernova community. Our main results are as follows.

(i) We significantly enlarge the SESN sample by adding 70 SESNe observed by LOSS.

(ii) We confirm that SESNe usually suffer moderately high extinction from their host galaxies. Quantitatively, we find a mean $E(B-V)$ value of 0.32 mag, substantially higher than the MW extinction, and also higher than that of SN Ia and SN II samples.

(iii) The peak *R*-band absolute magnitude of SESNe shows a wide range from −16 mag to brighter than −19 mag. SNe Ic-BL are more luminous than both SNe Ib and SNe Ic, and SNe Ic appear to be slightly brighter than SNe Ib.

(iv) SESNe exhibit smooth light-curve shapes with an ∼10–20 d rising phase before reaching maximum brightness, followed by a slow decay. A few SNe IIb show a decline dip at very early times

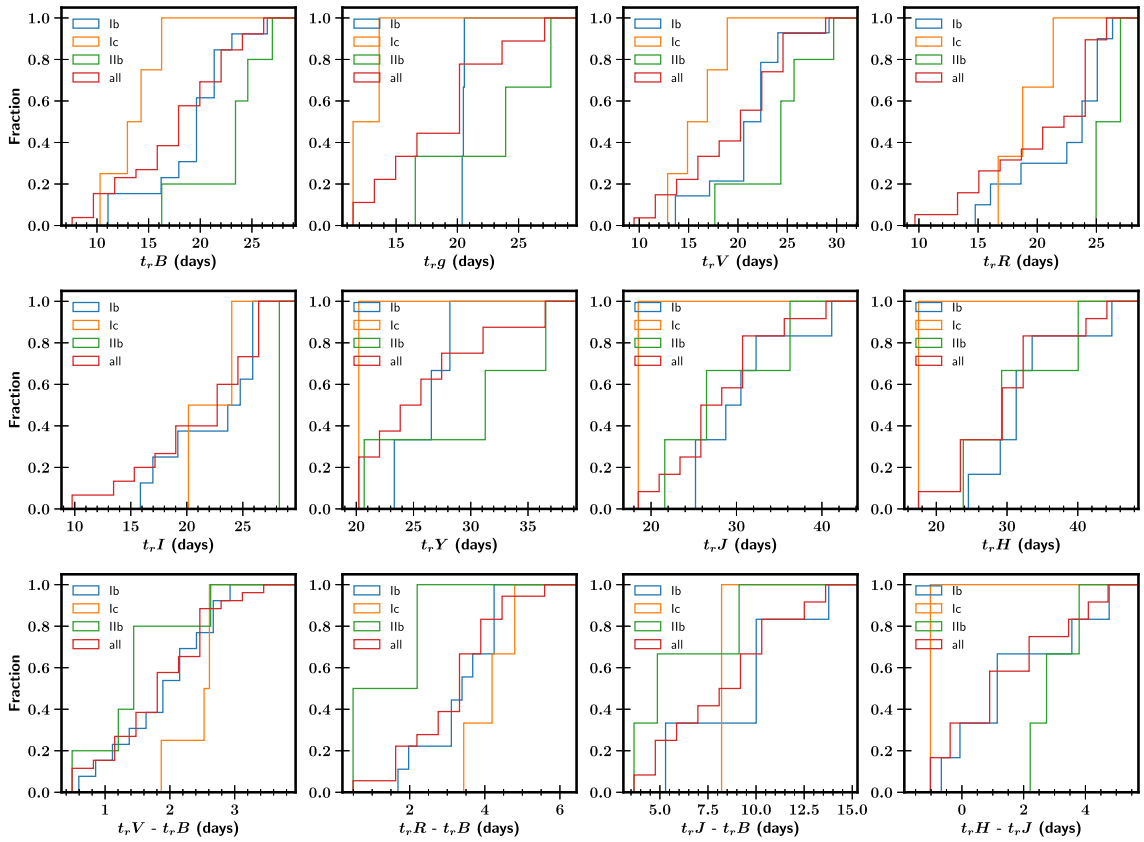

Figure 9. Top two rows: Cumulative distribution of rise time in eight different filters. K-S tests show significant differences between SNe Ib and SNe Ic, and also between SNe IIb and SNe Ib. The average rise times for SNe IIb, Ib, and Ic are 23.5, 19.9, and 13.8 d (respectively) in the *B* band. For almost all bands, SNe IIb have the longest rise time, while SNe Ic have the shortest rise time. Bottom row: The difference of rise time in the selected two bands. SNe Ic take more time for the redder band to reach peak after *B*-band peak compared to SNe IIb, opposite to the rise-time relation.

Table 6. The definitions, units, and prior ranges of the parameters of the fitting models.

Parameter	Definition	Unit	Posterior
	^{56}Ni model		
$M_{\rm ej}$	Ejecta mass	$M_\odot$	[0.1, 50]
v_9	Ejecta velocity	10^9 cm s^{-1}	[0.1, 5.0(10.0)]^a
$M_{\rm Ni}$	^{56}Ni mass	$M_\odot$	[0.001, 2.0(20.0)]^a
$\kappa_{\gamma,\,\rm Ni}$	Gamma-ray opacity of ^{56}Ni-cascade-decay photons	cm^2 g^{-1}	[0.027, 10^4]^c
$T_{\rm f}$	Temperature floor of the photosphere	10^3 K	[1000, 10, 000]
$t^{\rm b}_{\rm shift}$	Explosion time relative to the first data	days	[− 20, 0]
	Cooling model with three additional parameters compared to the ^{56}Ni model.		
$M_{\rm e}$	Envelope mass	$M_\odot$	[0.01, 30]
$R_{\rm e,\,12}$	Envelope radius	10^{12} cm	[10, 3000]
$E_{\rm e,\,50}$	Energy passed into the envelope from SN core	10^{50} erg s^{-1}	[10^{-5}, 10^3]^c
	Magnetar model with three different parameters compared to the ^{56}Ni model, but dropped $M_{\rm Ni}$ and $\kappa_{\gamma,\,\rm Ni}$.		
P_0	Initial period of the magnetar	ms	[0.8, 50]
$B_{\rm p,\,14}$	Magnetic field strength of the magnetar	10^{14} G	[0.1, 100]
$\kappa_{\gamma,\,\rm mag}$	Gamma-ray opacity of magnetar photons	cm^2 g^{-1}	[0.01, 10^4]^c

[a]For four luminous or superluminous SNe (SNe 2008fz, 2010hy, 2012aa, and 2018cow; see Table S3 in the supplementary material), the upper limits of prior of v_9 and $M_{\rm Ni}$ are set to be 10 and 20.0, respectively.
[b]For the SNe whose explosion date (t_0) had been inferred (see Table 5), the $t_{\rm shift}$ parameter was set to be fixed.
[c]Parameter was distributed in log space.

before rising again, which can be attributed to the shock-breakout cooling tail.

(v) For the first time, we derive reliable, robust measurements of the rise times for a large sample of SESNe in both optical and infrared bands. Our results show that SESNe rise faster in blue bands than in red bands.

(vi) Helium-poor SNe (SNe Ic) rise to maximum faster than helium-rich SNe (SNe Ib and IIb). Average rise times for SNe IIb,

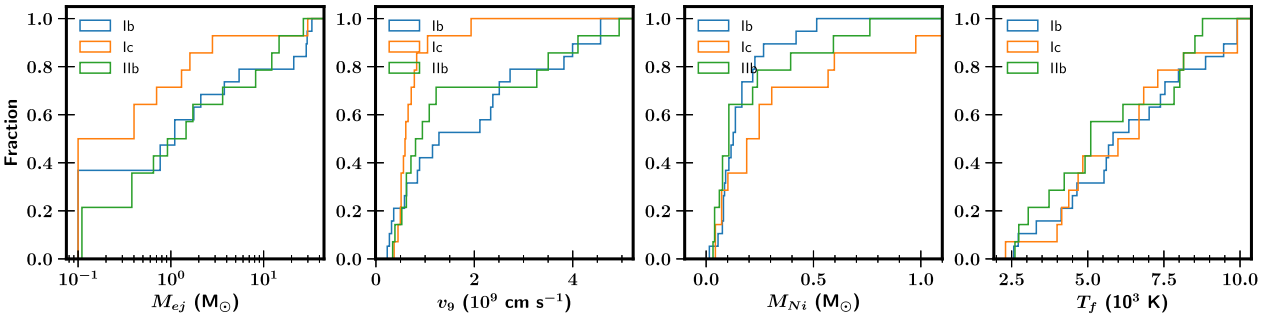

Figure 10. Cumulative distributions of the four parameters ($M_{\rm ej}$, v_9, $M_{\rm Ni}$, and $T_{\rm f}$) derived from model fitting. Compared to SNe Ib and SNe IIb, SNe Ic tend to have lower ejecta masses and also lower ejecta velocities, on average, but higher ^{56}Ni mass. The temperature floor of the photosphere distribution shows no significant difference between different subtypes.

Ib, and Ic are 23.5, 19.9, and 13.8 d (respectively) in the *B* band, and 26.1, 22.6, and 19.2 d (respectively) in the *R* band. K-S tests show significant differences between normal SNe Ib and SNe Ic, and also between SNe IIb and SNe Ib.

(vii) SNe Ic tend to have lower ejecta masses and also slower ejecta velocities, on average, compared to SNe Ib and SNe IIb, but with higher ^{56}Ni mass.

ACKNOWLEDGEMENTS

We thank Jenifer Rene Gross and Alessondra Springmann for their effort in taking Lick/Nickel data. We are grateful to the staff at Lick Observatory for their assistance with the Nickel telescope and KAIT. KAIT and its ongoing operation were made possible by donations from Sun Microsystems, Inc., the Hewlett-Packard Company, Auto Scope Corporation, Lick Observatory, the National Science Foundation (NSF), the University of California, the Sylvia & Jim Katzman Foundation, and the TABASGO Foundation. Research at Lick Observatory is partially supported by a generous gift from Google.

Support for AVF's supernova group has been provided by the NSF, Marc J. Staley (whose fellowship partly funded B.E.S. whilst contributing to the work presented herein as a graduate student), the Richard and Rhoda Goldman Fund, the TABASGO Foundation, Gary and Cynthia Bengier (who provided financial support for T.deJ. via the Bengier Postdoctoral fellowship), the Christopher R. Redlich Fund, and the UC Berkeley Miller Institute for Basic Research in Science (in which AVF was a Miller Senior Fellow at the time of this research). In addition, we greatly appreciate contributions from numerous individuals, including Charles Baxter and Jinee Tao, George and Sharon Bensch Greg and Patty Bernstein, Firmin Berta, Jack Bertges, Marc and Cristina Bensadoun, Greg and Patty Bernstein, Frank and Roberta Bliss, Ann and Gordon Brown, Eliza Brown and Hal Candee, Kathy Burck and Gilbert Montoya, Alan and Jane Chew, Christopher Cook, David and Linda Cornfield, Michael Danylchuk, Robert Davenport, Jim and Hildy DeFrisco, Alli and Byron Deeter, Tim and Melissa Draper, William and Phyllis Draper, Luke Ellis and Laura Sawczuk, Jim Erbs and Shan Atkins, Alan Eustace and Kathy Kwan, Art and Cindy Folker, Peter and Robin Frazier, David Friedberg, Harvey Glasser, Charles and Gretchen Gooding, Alan Gould and Diane Tokugawa, Richard Gregor, Thomas and Dana Grogan, Timothy and Judi Hachman Michael and Virginia Halloran, Gregory Hirsch and Kathy Long, Alan and Gladys Hoefer, Jerry and Patti Hume, Charles and Patricia Hunt, Stephen and Catherine Imbler, Adam and Rita Kablanian, Heidi Gerster Kikawada, Roger and Jody Lawler, Arthur and Rita Levinson, Jesse Levinson, Kenneth and Gloria Levy, Greg Losito and Ronnie Bayduza, Walter and Karen Loewenstern, Peter Maier, DuBose and Nancy Montgomery, Rand Morimoto and Ana Henderson, Sunil Nagaraj and Mary Katherine Stimmler, Peter and Kristan Norvig, James and Marie O'Brient, Emilie and Doug Ogden, Paul and Sandra Otellini, Margaret Renn, Robina Riccitiello, Leslie Roberts, Jeanne and Sanford Robertson, Paul Robinson, Eric Rudney, Sissy Sailors and Red Conger, Geraldine and David Sandor, Tom and Cathy Saxton, Stanley and Miriam Schiffman, Thomas and Alison Schneider, Ajay Shah and Lata Krishnan, Alex and Irina Shubat, Silicon Valley Community Foundation, Bruce and Debby Smith, Mary-Lou Smulders and Nicholas Hodson, Hans Spiller, Alan and Janet Stanford, Richard and Shari Stegman, Hugh Stuart Center Charitable Trust, Toby Stuart, Gerald and Virginia Weiss, Clark and Sharon Winslow, Ron and Geri Wohl, Weldon and Ruth Wood, David and Angie Yancey, Tom Zdeblick, and many others. XGW is supported by the National Natural Science Foundation of China (NSFC grant 11673006) and the Guangxi Science Foundation (grants 2016GXNSFFA380006 and 2017AD22006).

This research has made use of the NASA/IPAC Extragalactic Database (NED), which is operated by the Jet Propulsion Laboratory, California Institute of Technology, under contract with NASA. The Pan-STARRS1 Surveys (PS1) and the PS1 public science archive have been made possible through contributions by the Institute for Astronomy, the University of Hawaii, the Pan-STARRS Project Office, the Max-Planck Society and its participating institutes, the Max Planck Institute for Astronomy, Heidelberg and the Max Planck Institute for Extraterrestrial Physics, Garching, The Johns Hopkins University, Durham University, the University of Edinburgh, the Queen's University Belfast, the Harvard-Smithsonian Center for Astrophysics, the Las Cumbres Observatory Global Telescope Network Incorporated, the National Central University of Taiwan, the Space Telescope Science Institute, NASA under grant NNX08AR22G issued through the Planetary Science Division of the NASA Science Mission Directorate, the National Science Foundation grant AST-1238877, the University of Maryland, Eotvos Lorand University (ELTE), the Los Alamos National Laboratory, and the Gordon and Betty Moore Foundation. Funding for the Sloan Digital Sky Survey (SDSS) has been provided by the Alfred P. Sloan Foundation, the Participating Institutions, NASA, the NSF, the U.S. Department of Energy, the Japanese Monbukagakusho, and the Max Planck Society. The SDSS Web site is http://www.sdss.org/. The SDSS is managed by the Astrophysical Research Consortium (ARC) for the Participating Institutions. The Participating Institutions are The University of Chicago, Fermilab, the Institute for Advanced Study, the Japan Participation Group, The Johns Hopkins University, Los Alamos

National Laboratory, the Max-Planck-Institute for Astronomy (MPIA), the Max-Planck-Institute for Astrophysics (MPA), New Mexico State University, University of Pittsburgh, Princeton University, the United States Naval Observatory, and the University of Washington.

DATA AVAILABILITY

The data underlying this article are available in the article and in its online supplementary material.

REFERENCES

Anderson J. P., 2019, A&A, 628, A7
Arnett W. D., 1982, ApJ, 253, 785
Bazin G. et al., 2011, A&A, 534, A43
Bianco F. B. et al., 2014, ApJS, 213, 19
Burns C. R. et al., 2011, AJ, 141, 19
Cardelli J. A., Clayton G. C., Mathis J. S., 1989, ApJ, 345, 245
Chatzopoulos E., Wheeler J. C., Vinko J., 2012, ApJ, 746, 121
Conti P. S., 1975, Memoires of the Societe Royale des Sciences de Liege, 9, 193
Dai Z. G., Wang S. Q., Wang J. S., Wang L. J., Yu Y. W., 2016, ApJ, 817, 132
de Jaeger T. et al., 2019, MNRAS, 490, 2799
Drake A. J. et al., 2010, ApJ, 718, L127
Drout M. R. et al., 2011, ApJ, 741, 97
Eldridge J. J., Fraser M., Smartt S. J., Maund J. R., Crockett R. M., 2013, MNRAS, 436, 774
Filippenko A. V., 1988, AJ, 96, 1941
Filippenko A. V., 1997, ARA&A, 35, 309
Filippenko A. V., Matheson T., Ho L. C., 1993, ApJ, 415, L103
Filippenko A. V., Li W. D., Treffers R. R., Modjaz M., 2001, in Paczynski B., Chen W.-P., Lemme C., eds, ASP Conf. Ser. Vol. 246, IAU Colloq. 183: Small Telescope Astronomy on Global Scales.. Astron. Soc. Pac., San Francisco. p. 121
Foley R. J., Smith N., Ganeshalingam M., Li W., Chornock R., Filippenko A. V., 2007, ApJ, 657 L105
Foreman-Mackey D., Hogg D. W., Lang D., Goodman J., 2013, Publ. Astron. Soc. Pac., 125, 306
Fraser M. et al., 2021, preprint (arXiv:2108.07278)
Gal-Yam A., 2017, in Alsabti A., Murdin P., eds, Observational and Physical Classification of Supernovae. Springer, Cham, p. 195
Gal-Yam A. et al., 2014, Nature, 509, 471
Gal-Yam A. et al., 2021, Nature, 601, 7892
Ganeshalingam M., Li W., Filippenko A. V. et al., 2010, ApJS, 190, 418
Hosseinzadeh G. et al., 2017, ApJ, 836, 158
Kasen D., Bildsten L., 2010, ApJ, 717, 245
Kelly P. L., Kirshner R. P., Pahre M., 2008, ApJ, 687, 1201
Landolt A. U., 1983, AJ, 88, 439
Landolt A. U., 1992, AJ, 104, 340
Lang D., Hogg D. W., Mierle K., Blanton M., Roweis S., 2010, AJ, 139, 1782
Li W., Filippenko A. V., Chornock R., Jha S., 2003, Publ. Astron. Soc. Pac, 115, 844
Li W., Leaman J., Chornock R. et al., 2011, MNRAS, 412, 1441
Matheson T., 2001, PASP, 113, 1155
Modjaz M. et al., 2014, AJ, 147, 99
Nicholl M., Guillochon J., Berger E., 2017, ApJ, 850, 55
Pastorello A. et al., 2007, Nature, 447, 829
Pastorello A. et al., 2021, Transient Name Server AstroNote, 71, 1
Perley D. A. et al., 2022, ApJ, 927, 180
Piro A. L., Haynie A., Yao Y., 2021, ApJ, 909, 209
Podsiadlowski P., Joss P. C., Hsu J. J. L., 1992, ApJ, 391, 246
Poznanski D., Ganeshalingam M., Silverman J. M., Filippenko A. V., 2011, MNRAS, 415, L81
Poznanski D., Prochaska J. X., Bloom J. S., 2012, MNRAS, 426, 1465
Prentice S. J. et al., 2016, MNRAS, 458, 2973
Sana H. et al., 2012, Science, 337, 444
Schlafly E. F., Finkbeiner D. P., 2011, ApJ, 737, 103
Shivvers I. et al., 2019, MNRAS, 482, 1545
Smartt S. J., Eldridge J. J., Crockett R. M., Maund J. R., 2009, MNRAS, 395, 1409
Smith N., Owocki S. P., 2006, ApJ, 645, L45
Srivastav S., Smartt S. J., McBrien O., Smith K. W., Young D. R., Gillanders J., 2020, Transient Name Server Classification Report, 2020–2148, 1
Stahl B. E. et al., 2019, MNRAS, 490, 3882
Stahl B. E., Martínez-Palomera J., Zheng W., de Jaeger T., Filippenko A. V., Bloom J. S., 2020, MNRAS, 496, 3553
Stetson P. B., 1987, Publ. Astron. Soc. Pac., 99, 191
Stritzinger M., Suntzeff N. B., Hamuy M., Challis P., Demarco R., Germany L., Soderberg A. M., 2005, Publ. Astron. Soc. Pac., 117, 810
Stritzinger M. D. et al., 2018a, A&A, 609, A134
Stritzinger M. D. et al., 2018b, A&A, 609, A135
Taddia F. et al., 2015, A&A, 574, A60
Taddia F. et al., 2018, A&A, 609, A136
Tonry J. L. et al., 2012, ApJ, 750, 99
Valenti S. et al., 2011, MNRAS, 416, 3138
Van Dyk S. D., Hamuy M., Filippenko A. V., 1996, AJ, 111, 2017
Wang S. Q., Wang L. J., Dai Z. G., Wu X. F., 2015, ApJ, 807, 147
Woosley S. E., 2010, ApJ, 719, L204
Woosley S. E., Bloom J. S., 2006, ARA&A, 44, 507
Zheng W., Filippenko A. V., 2017, ApJ, 838, L4
Zheng W., Kelly P. L., Filippenko A. V., 2017, ApJ, 848, 66

SUPPORTING INFORMATION

Supplementary data are available at *MNRAS* online.

Figure S1: Same as Fig. 2, but in the natural system.
Figure S2: Model fitting of the 69 SNe with ^{56}Ni model.
Figure S3: Model fitting of the four SNe with the cooling model.
Figure S4: Model fitting of the four SNe with the magnetar model.
Table S1: Best-fitting parameters of the ^{56}Ni model for the SNe.
Table S2: Best-fitting parameters of the cooling plus ^{56}Ni model for the double-peaked SNe.
Table S3: Best-fitting parameters of the magnetar model for the luminous SNe.

Please note: Oxford University Press is not responsible for the content or functionality of any supporting materials supplied by the authors. Any queries (other than missing material) should be directed to the corresponding author for the article.

[1]*Department of Astronomy, University of California, Berkeley, CA 94720-3411, USA*
[2]*Department of Physics, University of California, Berkeley, CA 94720-7300, USA*
[3]*Institute for Astronomy, University of Hawaii, 2680 Woodlawn Drive, Honolulu, HI 96822, USA*
[4]*Miller Institute for Basic Research in Science, University of California, Berkeley, CA 94720, USA*
[5]*Guangxi Key Laboratory for Relativistic Astrophysics, School of Physical Science and Technology, Guangxi University, Nanning 530004, China*
[6]*Center for Interdisciplinary Exploration and Research in Astrophysics (CIERA) and Department of Physics and Astronomy, Northwestern University, 1800 Sherman Ave., Evanston, IL 60201, USA*
[7]*Department of Physics, Stanford University, Stanford, CA 94305, USA*
[8]*Department of Physics and Astronomy, University of California, Los Angeles, CA 90095, USA*
[9]*Department of Astronomy and Astrophysics, University of California Santa Cruz, 1156 High St., Santa Cruz, CA 95064, USA*

[10]*Department of Earth and Planetary Sciences, University of California Riverside, 900 University Ave., Riverside, CA 92521, USA*
[11]*Space Telescope Science Institute, 3700 San Martin Drive, Baltimore, MD 21218, USA*
[12]*Lawrence Berkeley National Laboratory, 1 Cyclotron Rd, Berkeley, CA 94720, USA*
[13]*Department of Astrophysical Sciences, Princeton University, 4 Ivy Lane, Princeton, NJ 08544, USA*
[14]*Netflix, Inc., 100 Winchester Cir, Los Gatos, CA 95032, USA*
[15]*Department of Physics, Florida State University, Tallahassee, FL 32306, USA*
[16]*Department of Astronomy & Astrophysics, The Pennsylvania State University, University Park, PA 16802, USA*
[17]*Institute for Computational & Data Sciences, The Pennsylvania State University, University Park, PA 16802, USA*
[18]*Institute for Gravitation and the Cosmos, The Pennsylvania State University, University Park, PA 16802, USA*
[19]*Jet Propulsion Laboratory, California Institute of Technology, Pasadena, CA 91109, USA*
[20]*The Aerospace Corporation, 2310 E. El Segundo Blvd., El Segundo, CA 90245, USA*
[21]*Center for Theoretical Physics, Department of Physics and Astronomy, Seoul National University, Seoul 08826, Korea*
[22]*Department of Physics and Astronomy, University of Wyoming, 1000 E. University, Dept. 3905, Laramie, WY 82071, USA*
[23]*Department of Physics and Astronomy, Johns Hopkins University, Baltimore, MD 21218, USA*
[24]*Department of Physics, University of California San Diego, La Jolla, CA 92093, USA*
[25]*Argonne National Laboratory, 9700 S. Cass Avenue, Lemont, IL 60439, USA*
[26]*Caltech/Spitzer Science Center, Caltech/IPAC, Mailcode 100-22, Pasadena, CA 91125, USA*
[27]*Department of Physics and Astronomy, University of Oklahoma, 440 W. Brooks St., Norman, OK 73019, USA*

This paper has been typeset from a TEX/LATEX file prepared by the author.